
Article:
Blereau, E orcid.org/0000-0001-8850-397X, Clark, C, Kinny, PD et al. (3 more authors) (2022) Probing the history of ultra-high temperature metamorphism through rare earth element diffusion in zircon. Journal of Metamorphic Geology, 40 (3). pp. 329-357. ISSN 0263-4929

https://doi.org/10.1111/jmg.12630

Blereau Eleanore (Orcid ID: 0000-0001-8850-397X)

Clark Chris (Orcid ID: 0000-0001-9982-7849)

Probing the history of UHT metamorphism through rare earth element diffusion in zircon

E. Blereau[1, 2*], C. Clark[1], P. D. Kinny[1], E. Sansom[1], R. J. M. Taylor[1, 3], M. Hand[4]

[1] *The Institute for Geoscience Research (TIGeR), School of Earth and Planetary Sciences, Curtin University, Perth 6845, Western Australia*

[2] *School of Earth and Environment, University of Leeds, Leeds LS2 9JT, United Kingdom (for future correspondence)*

[3] *Carl Zeiss Microscopy Ltd, ZEISS Group, Cambourne, Cambridge CB23 6DW, United Kingdom*

[4] *Centre for Tectonics, Resources and Exploration (TRaX), School of Earth and Environmental Sciences, University of Adelaide, SA 5005, South Australia*

*Corresponding author. Tel: +61 400 237 223

E-mail address: eleanore.blereau@gmail.com

This article has been accepted for publication and undergone full peer review but has not been through the copyediting, typesetting, pagination and proofreading process which may lead to differences between this version and the Version of Record. Please cite this article as doi: 10.1111/jmg.12630

Abstract

The extent to which solid-state volume diffusion modifies rare earth element (REE) abundances in accessory minerals during high-temperature metamorphism governs our ability to link recorded trace element compositions to particular thermal events. We model diffusion of REE in zircon under different temperature–time conditions and show that, for both short-lived (e.g. 1100°C for 1–5 Myr) and more prolonged (e.g. 1050ºC for 10–30 Myr or 1000ºC for 200 Myr) episodes of Ultra-High Temperature (UHT) metamorphism, REE diffusion in igneous zircon is sufficiently rapid for REE in a ~50 μm grain to equilibrate with the new metamorphic mineral assemblage of the host rock. By contrast, unless diffusion is accelerated by recrystallization, the presence of fluids or other processes, at temperatures below 900°C zircon will largely retain its original pre-metamorphic REE abundance pattern, even when the thermal event is long lived (≥100 Myr). Where volume diffusion is dominant, for instance in the absence of a fluid phase, the sensitivity of REE mobility to temperature can help constrain the temperature–time path of high-grade metamorphic rocks. Modelling of well-characterized natural samples from the regional-scale aureole surrounding the Rogaland Igneous Complex (RIC) in SW Norway shows that variations in REE concentration patterns in zircon indicate a *T–t* evolution that is consistent with independent *P–T–t* estimates for regional metamorphism based on phase equilibrium modelling (850–950ºC at 7–8 kbar for ~100 Myr). Greater modification of REE abundance patterns in zircons within 2 km of the RIC contact, however, indicates that UHT conditions persisted for ~150 Myr close to the intrusion, with a temperature of ~1100ºC for 1–5 Myr at the RIC contact. Thermal modelling suggests that the inferred *T–t* histories of samples from different distances from the RIC contact are best explained if the complex was emplaced incrementally over 1 to 5 Myr.

Keywords: zircon, diffusion modelling, rare earth elements, Rogaland Igneous Complex, polymetamorphism, geochronology.

1. INTRODUCTION

The partitioning of rare earth elements (REE) between minerals has become a widely-used petrochronological tool, linking isotopic age data to petrological observations indicative of particular geological events and/or processes. For example, the application of zircon–garnet REE partitioning has led to major advances in the interpretation of zircon U–Pb ages in garnet-bearing metapelitic and metabasic rocks (Rubatto, 2002; Rubatto & Hermann, 2007; Taylor et al., 2015; Taylor et al., 2017; Taylor, Kirkland, & Clark, 2016). However, zircon within high-grade and/or polymetamorphic rocks commonly record a complex spread of U–Pb ages, hampering the interpretation of the timescales of metamorphism (e.g. Taylor et al., 2020). In such rocks, there may be multiple generations of zircon, each preserving varying degrees of isotopic disturbance and recrystallization (Clark et al., 2015; Clark, Taylor, Kylander-Clark, & Hacker, 2018; Guevara et al., 2020; Halpin, Daczko, Milan, & Clarke, 2012; Harley, 2016; Harley, Kelly, & Möller, 2007; Kelly & Harley, 2005).

Trace-element equilibration between zircon and garnet during high-temperature metamorphic growth and/or recrystallization requires either the presence of fluid or melt, or sufficient time for solid-state diffusion to operate over length scales that exceeds grain size. Consequently, depending on the duration of the high-*T* metamorphic event(s), generations of zircon grains within nominally dry (melt-depleted) granulites may not fully (re-)equilibrate with garnet and/or other neighbouring REE-bearing minerals. Given the slow experimentally-determined rates of solid-state diffusion of REE (Cherniak & Watson, 2003), the recognition of partially modified REE patterns in zircon grains that have experienced prolonged high-*T* metamorphism offer the potential to constrain the temperature–time (*T–t)* history of rocks.

A natural laboratory in which to study these phenomena is the Rogaland–Vest Agder (RVA) Sector, part of the Sveconorwegian Belt in SW Norway. This terrain experienced prolonged high-*T* metamorphism during the Meso- to Neoproterozoic that culminated in the emplacement of a *c.* 930 Ma composite anorthosite massif, the Rogaland Igneous Complex (RIC) and the geographically associated Bjerkreim–Sokndal layered intrusion (Bingen, Davis, et al., 2008; Blereau et al., 2019; Blereau et al., 2017; Coint et al., 2015; Drüppel, Elsäßer, Brandt, & Gerdes, 2013; Laurent, Bingen, et al., 2018; Laurent, Duchene, Bingen, Bosse, & Seydoux-Guillaume, 2018; Laurent et al., 2016; Möller, O'Brien, Kennedy, & Kröner, 2003; Schärer, Wilmart, & Duchesne, 1996; Slagstad et al., 2018; Slagstad, Roberts, Marker, Røhr, & Schiellerup, 2013; Tomkins, Williams, & Ellis, 2005). In the aureole of the RIC (Figure 1), it is possible to study samples that experienced a wide range of peak metamorphic temperatures, combining both regional and contact metamorphic effects, and to compare and contrast their time-integrated geochemical responses.

The aims of this study are threefold. Firstly, we investigate systematically the variations in the REE compositions of zircon grains and compare these with modelled diffusion profiles, assuming equilibration between zircon and garnet, as an independent measure of their *T–t* evolution. Secondly, we differentiate between end-member models accounting for the *P–T–t* history of the RVA Sector by combining new *in situ* zircon and monazite geochronological data from samples collected over a range of distances from the RIC with existing petrological and *P–T* data from the same samples (Blereau et al., 2019; Blereau et al., 2017) and similar samples from other studies (e.g. Drüppel et al., 2013; Laurent, Bingen, et al., 2018; Laurent, Duchene, et al., 2018; Slagstad et al., 2018). Thirdly, we use the zircon REE data to model the thermal emplacement history of the RIC.

2. REGIONAL GEOLOGY

The detailed regional geology of the area has been summarized in a number of recent studies (Bingen et al., 2020; Blereau et al., 2017; Coint et al., 2015; Drüppel et al., 2013; Laurent, Duchene, et al., 2018; Laurent et al., 2016; Roberts & Slagstad, 2015; Slagstad et al., 2020; Slagstad et al., 2018; Slagstad, Roberts, & Kulakov, 2017; Slagstad et al., 2013; Spencer et al., 2014). In this paper we concentrate on the RIC and its country rocks.

The RIC is a c. 1000 km^2 anorthosite–mangerite–charnockite–granite plutonic complex. Its emplacement at *c.* 930–920 Ma RIC (Pasteels, Demaiffe, & Michot, 1979; Schärer et al., 1996; Westphal, Schumacher, & Boschert, 2003) resulted in a broad metamorphic aureole within which, historically, two approximately concentric and one essentially linear high-*T* mineral isograds have been identified (Tobi, Hermans, Maijer, & Jansen, 1985), marking the appearances of inverted pigeonite in orthogneiss, osumilite in paragneiss and orthopyroxene in the leucocratic portion of migmatites, respectively (Figure 1). However, recent studies have shown that the osumilite and orthopyroxene isograds are not true contact metamorphic isograds but rather the location of appropriate bulk compositions favourable to osumilite growth during both the regional and contact metamorphism, and an intrusional contact and/or the overprinting of several granulite-facies events in the case of orthopyroxene (Blereau et al., 2019; Coint et al., 2015).

Based largely on field relationships, the RIC is considered to record the sequential emplacement of three discrete anorthosite plutons and a layered intrusion (Marker, Schiellerup, Meyer, Robins, & Bolle, 2003; Schärer et al., 1996). Zircon grains associated with high-Al orthopyroxene megacrysts yielded statistically identical ages (929 ± 2, 932 ± 3 and 932 ± 3 Ma) for each of the three anorthosite plutonic phases (Schärer et al., 1996), which are typically interpreted as the age of emplacement of the RIC (Schärer et al., 1996; Slagstad et al., 2018). However, Sm–Nd dating of orthopyroxene megacrysts suggests that these grew much earlier

(*c.* 1040 Ma; Bybee et al., 2014), potentially indicating a more protracted emplacement and/or differentiation history (Ashwal & Bybee, 2017).

The regional upper amphibolite- to granulite-facies metamorphism associated with the Sveconorwegian Orogeny in the RVA Sector (M1; Tobi et al., 1985) followed a clockwise *P*–*T* path with maximum pressures of 7–8 kbars (Blereau et al., 2017; Drüppel et al., 2013; Jansen, Blok, Bos, & Scheelings, 1985) before undergoing near-isothermal decompression to *c.* 5 kbars (Blereau et al., 2017; Tomkins et al., 2005) prior to emplacement of the RIC. However, depending on the samples and methods employed, previous petrological and geochronological studies have reached different conclusions regarding the thermal evolution.

Most have argued for two distinct thermal peaks: (1) an early episode of regional metamorphism ('M1') that reached a peak of between ~700°C (Degeling, Eggins, & Ellis, 2001; Jansen et al., 1985; Tomkins et al., 2005) and 850–950°C (Blereau et al., 2017), either by *c.* 1035 Ma (Coint et al., 2015; Laurent, Bingen, et al., 2018; Laurent, Duchene, et al., 2018; Laurent et al., 2016; Tomkins et al., 2005) or significantly later by *c.* 1000 Ma (Möller, O'Brien, Kennedy, & Kröner, 2002; Möller et al., 2003), and; (2) a second thermal pulse ('M2') at *c.* 930 Ma associated with emplacement of the RIC, during which the rocks reached temperature of up to 900–1000°C (Blereau et al., 2017; Jansen et al., 1985; Laurent, Duchene, et al., 2018), consistent with the field evidence for a contact aureole superimposed on pre-existing regionally metamorphosed rocks (Tobi et al., 1985). An additional constraint on the timing of near-isothermal decompression between M1 and M2 is provided by a 955 ± 8 Ma age for zircon associated with the breakdown of garnet to cordierite (Tomkins et al., 2005). Importantly, within lithologies experiencing the second thermal pulse, some rocks remained melt present following heating due to the regional M1 metamorphism (Blereau et al., 2017), such that high temperature conditions were maintained throughout (Blereau et al., 2017; Slagstad et al., 2018). The key petrological evidence for a second thermal peak includes the growth of a secondary

generation of osumilite (Blereau et al., 2019) and garnet (Blereau et al., 2017), along with a variety of symplectitic or coronae reaction textures (Blereau et al., 2017, Laurent et al., 2018), as well as growth and resetting of accessory mineral geochronometers. In an alternative interpretation, Drüppel et al. (2013) argued for a single regional UHT peak of ~1000°C at *c.* 1010 Ma, and interpreted xenotime ages of *c.* 930 Ma as relating to melt crystallization during post-decompressional cooling rather than to a discrete thermal overprint.

Lower-grade retrograde effects with recorded ages down to 908 ± 9 Ma have been designated M3 and ascribed to cooling of the RIC (Maijer, 1987; Möller et al., 2003; Westphal et al., 2003). Importantly, this part of southern Norway was relatively unaffected by subsequent Caledonian tectonothermal events (Verschure et al., 1980). Table 1 summarizes existing U–Pb age data on which these interpretations are largely based.

3. SAMPLE DESCRIPTION

Accessory minerals and garnet from five samples from the RVA Sector were analysed for U–Pb geochronology and trace-element geochemistry. Three samples were collected from the regionally metamorphosed metapelitic country rocks at various distances from the RIC contact: sample ROG13/11 at ~30 km; sample ROG13/10 at ~10 km, and sample ROG13/2 at ~2 km from the contact. The other two samples, a metapelite (ROG14/5) and an anorthosite sheet (ROG14/8), were collected a few metres from the main contact (Figure 1b). The petrology of three of these samples (ROG13/11, ROG13/10 and ROG14/5) was discussed in detail by Blereau et al. (2017) and is summarized here, together with descriptions of the two additional samples. We provide details on the morphology of zircon and monazite from all samples.

3.1 Garnet–sillimanite–cordierite migmatite (ROG13/11)

This migmatitic metapelite, collected some 30 km from the RIC contact (Figure 1b), is composed of a foliated melanosome rich in garnet, sillimanite and cordierite together with quartzofeldspathic stromatic leucosomes containing peritectic garnet (Blereau et al., 2017). Zircon grains occur within the leucosome and melanosome as equant to slightly elongate grains 25–200 μm long. Some of the grains contain oscillatory-zoned cores with bright cathodoluminescence (CL) response that are surrounded and sometimes truncated by overgrowth rims of dark CL response (Figure 2a i, ii). Other grains show internal features commonly associated with recrystallization, including diffuse, remnant oscillatory zoning (Figure 2a iii, iv), that resembles the 'ghost textures' of Hoskin and Black (2000), and a dark CL response. Monazite (40–100 μm) occurs throughout the sample as inclusions in or around the margins of garnet, cordierite, sillimanite, ilmenite and K-feldspar. The studied grains appear uniform in backscattered electron (BSE) images (Figure 2f).

3.2 Sapphirine–orthopyroxene–cordierite–spinel granulite (ROG13/10)

This residual, silica-undersaturated, sapphirine-bearing granulite (paragneiss) was collected from near Ivesdalen, approximately 10 km from the RIC (Blereau et al., 2017) (Figure 1b), and is the same locality as sampled by Drüppel et al. (2013), Laurent, Bingen, et al., (2018) and Laurent, Duchene, et al., (2018). Zircon (20–100 μm) occurs throughout as inclusions within or around the margins of cordierite, biotite, orthopyroxene and spinel. Grain shapes vary from equant to elongate. Zircon grains contain bright CL response oscillatory-zoned cores (Figure 2b i, ii) as well as more diffuse 'ghost zoning' (Hoskin & Black, 2000) indicative of recrystallization (Figure 2b iii, iv). Some grains have uniform areas with dark CL response that appear to truncate the zoning of the bright CL cores (Figure 2b i, ii), and are interpreted to have recrystallized. No monazite was found in this sample.

3.3 Osumilite–orthopyroxene–spinel migmatite (ROG13/2)

This osumilite-bearing migmatite is from near Vikeså, approximately 2 km from the RIC (Figure 1b), and is the same locality sampled by Laurent et al. (2016), Slagstad et al. (2018) and Blereau et al. (2019). The rock consists of melanosome containing osumilite, orthopyroxene, spinel, garnet, quartz and feldspar, and leucosome containing quartz, orthopyroxene, K-feldspar (perthite) and plagioclase. Osumilite occurs as large, irregularly shaped, pale purple grains (~1 cm; Blereau et al., 2019) that are colourless to pale pink in thin section; some contain inclusions of spinel/magnetite and garnet (~0.2 mm) (Figure 3a, b). A second generation of osumilite forms coronas around garnet (Blereau et al., 2019). Osumilite also occurs in fine-grained symplectites along with quartz and cordierite. (Figure 3d, e). Orthopyroxene occurs in trails of grains 0.5–4 mm across that are aligned parallel to the foliation and contain inclusions of quartz, spinel/magnetite, ilmenite and biotite. Quartz occurs as large elongate grains (~4–6 mm) in the leucosome as well as smaller grains (~1 mm) in the melanosome. Cordierite occurs as rare grains in osumilite, and in symplectites in which it is intergrown with K-feldspar + quartz ± orthopyroxene, and which contain inclusions of opaque minerals/spinel and biotite (Figure 3b, d). These symplectites likely represent pseudomorphs after osumilite (Figure 3 b, d) (Bhattacharya & Kar, 2002; Ellis, Sheraton, England, & Dallwitz, 1980; Holder, Hacker, Horton, & Rakotondrazafy, 2018; Kelsey, 2008; Korhonen, Brown, Clark, & Bhattacharya, 2013a). Minor inclusions (~0.1 mm) of biotite occur in K-feldspar and in association with opaque inclusions in cordierite.

Zircon grains in this sample vary in size (50–200 μm) and shape and show complex internal structures in CL. Grains either contain oscillatory-zoned cores (Figure 2c ii) or partially recrystallized cores with diffuse oscillatory zones that are truncated and surrounded by uniform overgrowths (Fig 2c iii, v). One sector-zoned grain was also analysed (Figure 2c iv).

Overgrowths show variable CL response from (relative to cores) dark (Figure 2c, i) to bright (Figure 2c iii, v). The few grains of monazite (100–400 μm) recovered from the sample show no internal variation in BSE images (Figure 2g).

3.4 Garnet–sillimanite–cordierite–spinel migmatite (ROG14/5)

This migmatitic garnet–sillimanite–cordierite–spinel metapelitic gneiss is located at the contact of the RIC (Figure 1b). The sample consists of melanosome rich in garnet and cordierite and millimetre-scale leucosomes (Blereau et al., 2017). Zircon grains (60–200 μm) have multifaceted 'soccer ball' morphologies indicating metamorphic recrystallization (Vavra, Gebauer, Schmid, & Compston, 1996). Internally, they are either sector-zoned (Figure 2d i, iv) or display diffuse convoluted zoning to simple zoning in their CL response (Figure 2d ii, iii). Monazite grains are similar in size (100–200 μm) to zircon, and many contain sillimanite inclusions (Figure 2h i). A number of monazite grains show minor brightness variation in BSE images (Figure 2h i, ii, iv), most likely due to variations in Th content.

3.5 Garnet-bearing anorthosite (ROG14/8)

This sample was collected from the same locality as ROG14/5 (Figure 1b) and is one of a series of garnet-bearing anorthosite sheets (~0.3–2 m long, ~5–10 cm wide) that intrude the country rock (garnet–sillimanite–spinel–cordierite metapelitic gneiss) adjacent to the main RIC contact (Figure 4a). The anorthosite sheets are parallel to the foliation in the surrounding migmatite. The sample is dominated by equant, 1–2 mm subhedral plagioclase that shows minor sericitization (Figure 4b, c). Orthopyroxene occurs in millimetric layers as subhedral to anhedral grains of variable size (1–8 mm) (Figure 4b, c). Garnet forms clusters of small, subhedral, inclusion-free grains (<1 mm) and larger, euhedral grains (~1.5 mm) (Figure 4b). Ilmenite (~0.5 mm), biotite (~1 mm) and quartz (1–2 mm) are minor phases.

Only zircon was analysed from this sample as monazite grains were too small to analyse. The zircon grains (50–300 μm) mostly have oscillatory-zoned cores (Figure 2e i, ii, iv), although some showing more diffuse zoning with low CL response (Figure 2e iii). The cores are surrounded and sometimes crosscut by sector-zoned to uniform regions with brighter CL response (Figure 2e iv). A few grains have overgrowths with darker CL response (Figure 2e i, iii).

4. METHODS

4.1 Diffusion modelling

Theoretical profiles for REE diffusion within zircon were generated using a custom Python program. As a starting condition, our modelling assumed a compositionally homogenous zircon characterised by a typical igneous REE composition (C_O) comprising a steep middle to heavy REE (M–HREE) profile ($Gd_N = 110$; $Lu_N = 1000$). Diffusion of the REE was simulated under different temperature–time scenarios, and assumed a final (equilibrated) compositional profile (C_{Eq}; a simplified flat M–HREE profile with all elements at 110 times chondritic abundance) consistent with zircon in equilibrium with garnet (e.g. Rubatto, 2002; Hokada and Harley, 2004; Rubatto and Herman, 2007; Taylor et al., 2014; Taylor et al., 2015; Taylor et al., 2017). This approach assumes that the systems under consideration contained garnet throughout their high-temperature metamorphic evolution. For simplicity we assumed a spherical grain with a radius (r) of 50 μm, and assumed volume diffusion as the only process acting to modify the composition of the grains, with the REE diffusing outwards into an infinite volume.

The model does not integrate possible contributions to diffusion rates from other factors such as the presence of fluids or radiation damage. Metamorphic rocks in Rogaland are particularly residual due to having experienced two high-grade metamorphic and melt-loss

events, with no evidence for fluid mediated alteration (e.g. coupled dissolution reprecipitation) of accessory minerals and minimal growth of new metamorphic zircon, increasing the action of diffusional processes. Radioactive decay causes damage to mineral lattices over time, increasing the diffusivity of elements and potentially forming inverse zoning (e.g. Laurent, Bingen et al., 2018). However, high-temperature metamorphism can repair such damage through annealing (Kusiak et al., 2015; Nasdala et al., 2001). This model does not consider changes to the light REE (La–Eu) as they are not systematically related between zircon and garnet as well as have low concentrations. These assumptions are based on the ubiquity of garnet, the residual, nominally anhydrous nature of the samples analysed in this study, and the high-grade, prolonged polymetamorphic history of the region under which conditions we argue volume diffusion would have dominated.

To calculate the modified REE concentrations, C, at radial distance, a (where $a \leq r$) for time intervals, t, between 0.5–200 Myr, and for temperatures in the range 850–1100°C, the following equation from Crank (1975, 2nd edition) was used:

$$C = C_O \times \frac{1}{2}\left\{erf\left[\frac{a+r}{2\sqrt{(Dt)}}\right] + erf\left[\frac{a-r}{2\sqrt{(Dt)}}\right]\right\}$$

$$-\left\{\left(\frac{1}{r}\right)\sqrt{\left(\frac{Dt}{\pi}\right)} \times \left(exp\left[\frac{-(a-r)^2}{4Dt}\right] - exp\left[\frac{-(a+r)^2}{4Dt}\right]\right)\right\}$$

If the equilibrium concentration, C_{Eq}, for a diffusing element was reached, the concentration of that element was held constant for the remainder of the run. The REE diffusion coefficients (D in m^2s^{-1}) applied in the calculations were average values calculated using the Arrhenius functions of Cherniak, Hanchar, and Watson (1997). For Dy and Yb these coefficients were calculated directly; for the remaining M–HREE, D values were extrapolated from those experimental data using the polynomial relationships between ionic radius (IR),

activation energy (E_a) and pre-exponential factor (D_0) from Cherniak et al. (1997) (see Table S1).

We chose not to model diffusivity of Pb as its behaviour in high-*T* zircon is poorly understood (Kusiak et al., 2015; Kusiak, Whitehouse, Wilde, Nemchin, & Clark, 2013; Peterman et al., 2016; Whitehouse, Kusiak, Wirth, & Ravindra Kumar, 2017). Available experiments on Pb diffusion in zircon report diffusivities similar to or faster than those of the HREE (Cherniak & Watson, 2001; Lee, Williams, & Ellis, 1997) and cannot account for the presence of features such as Pb nanospheres that effectively halt radiogenic Pb loss (Kusiak et al., 2015; Whitehouse et al., 2017). Pb nanoclusters have been found in zircon from Rogaland previously (Laurent, Bingen, et al., 2018), but no associated clustering of REE has been recognised (Kusiak et al., 2015; Kusiak et al., 2013; Whitehouse et al., 2017).

4.2 Analytical methodology

The methodology for SHRIMP (U–Pb geochronology) and LA–ICP–MS/LASS (REE geochemistry) analyses can be found within Supplementary Appendix S1. All sample preparation and analytical work was conducted using facilities within the John de Laeter Centre, Curtin University and included utilisation of the SelFRAG Electric Pulse Disaggregation (EPD) unit, Tescan Mira3 Field Emission Scanning Electron Microscope (FESEM), SHRIMP II A ion microprobe and GeoHistory Facility LA–ICP–MS.

4.3 Thermal modelling

Two-dimensional thermal models for the emplacement of the RIC were generated using the HEAT 3D program (Wohletz, Civetta, & Orsi, 1999; see: http://www.lanl.gov/orgs/ees/geodynamics/Wohletz/KWare/Index.htm), which solves the heat transfer equation in multiple dimensions using the parameters summarized in Table S2. The

program quantifies heat flow around a magma body and predicts the changes in temperature due to contact metamorphism. These models were used to estimate the *T–t* evolution of samples at different distances from the RIC for different pluton emplacement scenarios. The initial linear geothermal gradient used for the country rocks (44°C/km) was based on the petrological and peak regional metamorphic *P–T* constraints of Blereau et al. (2017).

5. RESULTS

5.1 Zircon U–Pb Geochronology

Zircon U–Pb data are provided in Supplementary Data Table S3, and concordia plots summarizing the results in Figure 5. Analyses are considered to be concordant if their 2σ error ellipse overlaps with the concordia curve (Spencer, Kirkland, & Taylor, 2016).

5.1.1 Garnet–sillimanite–cordierite migmatite (ROG13/11 – 30 km)

Fifteen U–Pb analyses on zircon grains from sample ROG13/11 form a mixing array of concordant to slightly discordant data (Figure 5a). The oldest ages, up to 1917 ± 6 Ma ($^{207}Pb/^{206}Pb$), were obtained from oscillatory-zoned cores, which have Th/U ratios of 0.23–0.77, typical of magmatic zircon. Zones showing diffuse oscillatory zoning have lower Th/U ratios of 0.03–0.18, supporting an interpretation that they represent original oscillatory-zoned cores that underwent recrystallization. These give younger $^{206}Pb/^{238}U$ dates extending down to 1009 ± 15 Ma. Three zircon rims with similar low Th/U ratios (0.03–0.11) form a concordant group with a weighted mean $^{206}Pb/^{238}U$ age of 957 ± 15 Ma (MSWD = 0.62, prob. = 0.54). Overall, the data can be interpreted as detrital zircon cores of various ages that underwent variable degrees of Pb loss and recrystallization during metamorphism at *c.* 1000 Ma, with subsequent neocrystallization of zircon on rims of existing grains at 957 ± 15 Ma.

5.1.2 Sapphirine–orthopyroxene–cordierite–spinel granulite (ROG13/10 – 10 km)

Twenty-seven U–Pb analyses on zircon grains from sample ROG13/10 also form a mixing array of concordant to slightly discordant analyses extending down to *c.* 1000 Ma (Figure 5b). Again, the oldest ages, up to 1549 ± 19 Ma ($^{207}Pb/^{206}Pb$), were obtained from oscillatory-zoned cores with Th/U ratios in the range 0.21–0.40. Similarly, zones showing textures indicative of recrystallization and with generally lower values of Th/U ratios (0.09–0.32) yielded the youngest dates. Among these, two uniform recrystallized domains yielded the youngest $^{206}Pb/^{238}U$ ages of 1076 ± 12 and 1055 ± 13 Ma. No distinctly younger zircon rims were found.

5.1.3 Osumilite–orthopyroxene–spinel migmatite (ROG13/2 – 2 km)

Eleven U–Pb analyses on zircon grains from ROG13/2 yielded a similar age range to the previous two samples, albeit extending to a somewhat younger age limit of *c.* 900 Ma (Figure 5c). Together, oscillatory-zoned cores and recrystallized parts of grains (Th/U = 0.12–1.02) yielded $^{206}Pb/^{238}U$ ages ranging from 1574 ± 27 to 1011 ± 18 Ma. Three analyses of zircon overgrowths with variable CL response and a wide range of Th/U (0.54–1.08), yielded a weighted mean $^{206}Pb/^{238}U$ age of 920 ± 13 Ma (MSWD = 1.7, prob. = 0.18), whereas a single analysis of a sector-zoned zircon yielded the youngest $^{206}Pb/^{238}U$ age of 899 ± 15 Ma and an exceptionally high Th/U ratio of 2.79.

5.1.4 Garnet–sillimanite–cordierite–spinel migmatite (ROG14/5 – ~10 m)

Eight U–Pb analyses on either recrystallized oscillatory-zoned or sector-zoned domains within zircon grains from sample ROG14/5 produced a much narrower age range than the previously described samples (Figure 5d). All analyses were characterized by low Th/U ratios (0.02–0.14) and had $^{206}Pb/^{238}U$ ages ranging from 1025 ± 15 to 919 ± 18 Ma.

5.1.5 Garnet-bearing anorthosite (ROG14/8 – ~10 m)

Twenty-nine U–Pb analyses on zircons from the anorthosite sheet sample ROG14/8 (Figure 5e), were mostly of recrystallized zircon with diffuse oscillatory zoning and Th/U ratios of 0.09–0.51. These analyses yielded $^{206}Pb/^{238}U$ ages ranging from 1017 ± 11 to 926 ± 12 Ma. Two unzoned zircon cores with weak CL response (Th/U = 0.25–0.50) recorded slightly older $^{206}Pb/^{238}U$ ages of 1045 ± 17 and 1036 ± 11 Ma. Three overgrowths with weak CL response and Th/U of 0.59–0.72 yielded the youngest ages that define a combined weighted mean $^{206}Pb/^{238}U$ age of 917 ± 12 Ma (MSWD = 0.21, prob. = 0.81).

5.2 Monazite U–Pb geochronology

Monazite U–Pb analyses can be found in Supplementary Data Table S4. Concordia plots summarizing the results are presented in Figure 6, on which analyses are shaded according to their Th/U ratio. In all three monazite samples there is a tendency for those analyses recording the youngest apparent ages to have the highest Th/U.

5.2.1 Garnet–sillimanite–cordierite migmatite (ROG13/11 – 30 km)

Eighteen U–Pb analyses of monazite grains plot within error of concordia (Figure 6a) and show a comparatively narrow range of $^{206}Pb/^{238}U$ ages from 1038 ± 11 to 960 ± 11 Ma (Th/U = 1.6–40). Among these, the twelve oldest analyses form a cluster of overlapping error ellipses with a weighted mean $^{206}Pb/^{238}U$ age of 1028 ± 7 Ma (MSWD = 0.37, prob. = 0.96).

5.2.2 Osumilite–orthopyroxene–spinel migmatite (ROG13/2 – 2 km)

Seven U–Pb analyses of monazite grains form a similar overall array to the monazites analysed in ROG13/11, with $^{206}Pb/^{238}U$ ages ranging from 1037 ± 11 to 983 ± 12 Ma (Th/U = 2.2–40) (Figure 6b).

5.2.3 Garnet–sillimanite–cordierite–spinel migmatite (ROG14/5 – ~10 m)

Eighteen U–Pb analyses of monazite grains form an array of data that extends to significantly younger ages than either of the previous two samples (Figure 6c), with $^{206}Pb/^{238}U$ ages range from 990 ± 11 to 886 ± 11 Ma (Th/U = 10–88).

5.3 Trace-element geochemistry

Rare earth element and yttrium abundances were measured from areas of zircon and monazite grains with concordant U–Pb ages in all garnet-bearing samples (i.e. excluding sample ROG13/10). Garnet grains were analysed in thin section or, in one case (ROG13/2) from a mineral separate, and targeted any texturally distinct cores and rims. Results are summarized on chrondrite-normalised REE plots in Figures 7 and 8, and in Supplementary Data Tables S5–S7. To distinguish the different morphological types of zircon analysed, in Figure 7a–d the same colour scheme was used on as in Figure 5a–e.

5.3.1 Zircon REE

ROG13/11 (30 km). The overall range of compositions for zoned cores and recrystallized areas is similar, with chondrite-normalised Lu contents (Lu_N) of 486–2350 and Yb_N/Gd_N ratios of 5.1–12.4 (Figure 7a). A rim with dark CL response has a steeper slope (Yb_N/Gd_N = 122) and higher HREE abundances (Lu_N = 6780 as compared to 486–2350).

ROG13/2 (2 km). The oscillatory zoned cores and one older recrystallized area ($^{206}Pb/^{238}U$ age 1476 ± 19 Ma) collectively yielded Yb_N/Gd_N ratios of 6.9–16.8 (Figure 7b), similar to the majority of zircons in sample ROG 13/11. The remaining recrystallized zircon, sector-zoned zircon and three younger rims yielded flatter patterns (Yb_N/Gd_N = 0.74–5.5).

ROG14/5 (~10 m). All of the analysed zircons, majoritively recrystallized areas, record Yb_N/Gd_N ratios of 0.22–0.82 (Figure 7c). HREE abundances are consistently lower than in the previous two samples (Lu_N = 41.6–63.0) and show less variability.

ROG14/8 (~10 m). The majority of zircon analyses record a similar range of compositions with Lu_N = 971–5070 and Yb_N/Gd_N = 5.6–52.4 (Figure 7d). The exception was one sector-zoned core that yielded a pattern with a similarly negative slope (Yb_N/Gd_N = 0.5) and low HREE concentration (Lu_N = 60.1) to the zircons from adjacent sample ROG14/5.

5.3.2 Garnet REE

ROG13/11 (30 km). Garnet from various textural settings in this migmatite were analysed, with Grt1 in the melanosome and Grt2 in the leucosome. A range of M–HREE patterns were obtained (Figure 7e). The core of a large Grt1 porphyroblast containing abundant sillimanite inclusions shows a hump-shaped M–HREE pattern, with relatively elevated concentrations of Tb and Dy decreasing steeply to Lu (Lu_N = 35.8–68.7). Analyses of the inclusion-free rim are similar in shape but have higher HREE contents (Lu_N = 114–334). Rims of Grt1 garnets that are partly resorbed and replaced with cordierite ('resorbed Grt1'), have the highest M–HREE concentrations (Lu_N = 348–591) (Figure 7e). In contrast to Grt1, the inclusion-rich core of a large peritectic Grt2 shows a positive M–HREE slope (Yb_N/Gd_N = 3.9–4.6; Lu_N 377–679),

whereas the inclusion-free rims have flat to slightly convex M–HREE patterns (Yb_N/Gd_N = 0.9–1.2; Lu_N = 86.4–123).

ROG13/2 (2 km). Garnet is relatively scarce in this sample. Grt1 is a relict garnet inclusion in osumilite (Figure 3a) with a positive M–HREE slope (Yb_N/Gd_N = 23.1–23.7), flattening towards the HREE which are present in very high abundance (Lu_N > 26000) (Figure 7f). Garnet recovered from a mineral separate (Grt2) yielded a shallower positive M–HREE slope (Yb_N/Gd_N = 8.4–9.1), with lower concentration flat HREE patterns (Lu_N = 2910–5140). Concentrations were somewhat higher at the rim (Lu_N = 5135).

ROG14/5 (~10 m). There is textural evidence for two generations of garnet in the melanosome, with secondary garnet (Grt2) nucleated on primary garnet grains (Grt1) as well as on ilmenite and spinel-magnetite. The abundance patterns for both generations are similar, with flat to slightly bowed shapes (Yb_N/Gd_N = 0.9–2.7) (Figure 7g). Grt1 has somewhat higher M–HREE abundances than Grt2.

ROG14/8 (~10 m). Two distinct sizes of garnet have contrasting REE patterns. Larger euhedral garnets (Grt1) show nearly flat M–HREE slopes (Figure 7h) (Yb_N/Gd_N = 1.8–3.6). The rims of these grains have slightly higher HREE abundances (Lu_N = 532–905) than the cores (Lu_N = 410–540). Smaller subhedral garnets (Grt2) show positive M–HREE slopes (Yb_N/Gd_N = 16.5–18.5) leading to higher overall HREE concentrations (Lu_N = 3210–4150) than in Grt1.

5.3.3 Monazite REE

All monazite analyses display typical chondrite-normalised REE patterns (Figure 8), with negative Eu anomalies and steeply negative M–HREE slopes. The patterns from

ROG13/11 and ROG14/5 are similar in terms of the degree of slope (Yb_N/Gd_N = 0.001–0.02) and size of the Eu anomaly (Eu/Eu* = 0.01–0.12), whereas the pattern for ROG13/2 shows a less steep negative slope (Yb_N/Gd_N = 0.02–0.16), and a smaller Eu anomaly (Eu/Eu* = 0.13–0.73).

6. DISCUSSION

6.1 Modification of REE during high-*T* conditions

Accessory mineral REE abundances can be used to relate zircon and monazite U–Pb ages to the bulk silicate mineral assemblage, and potentially to identify modification by processes such as fluid-mediated dissolution–reprecipitation (Kelly, Harley, & Möller, 2012; Rubatto, 2017; Taylor et al., 2014). Although there are only empirical estimates for REE partitioning between monazite and garnet, experimentally-quantified zircon–garnet REE partitioning data are available for a limited range of *P–T* conditions (Rubatto & Hermann, 2007; Taylor et al., 2015). The experimental conditions of Taylor et al. (2015) are applicable to the extreme crustal conditions within the RIC, making it possible to interpret zircon-garnet equilibrium in these rocks. Pure volume diffusion of trace-elements in zircon is slow compared to many other common minerals (Cherniak et al., 1997), and recrystallized zircon within a garnet-bearing rock may never equilibrate with garnet, although where garnet is stable newly-grown metamorphic zircon should. In addition, the REE in zircon diffuse at different rates (HREE > MREE > LREE) (Cherniak et al., 1997). In recrystallized zircon, this can result in complex data sets due to variably incomplete modification of the different REE within any given analytical volume (Taylor et al., 2016).

In order to determine the relationship between REE and the conditions and timescales of metamorphism, theoretical diffusion profiles for Gd to Lu were calculated to model the changes in REE composition that would be expected during the modification of an originally

igneous zircon (with steep M–HREE; C_O) to a modified REE composition in equilibrium with garnet (flat M–HREE; C_{Eq}) for different thermal conditions and timescales (Figure 10). Figure 9 shows how the modelled diffusion profiles for Dy and Yb from core to rim change with time at different temperatures. Values for Gd to Lu were extrapolated from each element's respective profile (Figure 10, Table S8). Figure 10 shows the M–HREE composition that would be sampled by an in-situ analysis, assuming a 20 μm spot diameter, on the very edge of the model zircon for different temperatures and timescales.

The modelling shows that for temperatures of 850–900°C, even after 100 Myr or longer, little to no modification to the M–HREE is expected at the edge of the grain (Lu decreases by ~2–20%, compared to Ho which decreases by ~1–4%) (Figure 10). This implies that, as long as volume diffusion is the only process acting, REE within recrystallized zircon from rocks experiencing such conditions will preserve the original (igneous) compositions. Prolonged periods (≥100 Myr) at 950°C results in a significantly greater REE modification compared to at 900°C (Ho from 4% to 21% and Lu from 18% to 63%), but does not cause complete M–HREE equilibration within the analytical volume. However, at more extreme temperatures (e.g. 1050ºC), even short periods (10 Myr) reduce the concentration of all M–HREE by ≥85% (86% for Ho and >99% for Lu), resulting in near flat patterns (Figure 10). At 1050ºC, complete equilibration of M–HREE in zircon (i.e. flat model M–HREE patterns) occurs within 10–30 Myr, and at 1100°C equilibration is achieved within 1–5 Myr (Figure 10). Therefore, 1000°C appears to be a key threshold above which complete modification of all REE can occur on plausible orogenic timescales (e.g. < 200 Myr: Clark et al., 2018; Harley, 2016; Korhonen, Clark, Brown, Bhattacharya & Taylor, 2013b; Taylor, Johnson, Clark & Harrison, 2020).

In order to demonstrate the effect of variable REE diffusion within zircon under different *T–t* conditions as well as more variable analytical spot placement, simulated traverses of 20 μm analytical spots from core to rim were generated from the various modelled zircon

diffusion profiles (Figure 11a–f) (Table S8). Under granulite-facies conditions (<900ºC), the modified REE profiles confirm that the M–HREE are largely immobile (Cherniak et al., 1997), with the simulated zircon essentially retaining its original REE signature across the profile despite prolonged high-*T* conditions (850–900°C for <100 Myr) (Figure 10, 11a–b).

6.2 Metamorphic events in SW Norway

Blereau et al. (2019) argued that prograde high–*T* regional metamorphism in the RVA sector occurred at *c.* 1070 Ma, based on the earliest $^{40}Ar/^{39}Ar$ age of osumilite from sample ROG13/2, matching some of the earliest recorded metamorphic zircon U–Pb ages from a number of studies (Table 1). Given the complexity of the metamorphic history of the RVA, determining the precise timing of peak metamorphism has proven more problematic. Detrital zircon, from the metasedimentary samples located between 2 and 30 km from the RIC (Blereau et al., 2017) show variably recrystallized textures with concomitant isotopic resetting (Figure 5), which result in discordia arrays that converge at *c.* 1000 Ma or younger (Figure 12). Similar age spreads have been found in a number of previous studies (Drüppel et al., 2013; Laurent, Bingen, et al., 2018; Möller et al., 2002; Möller et al., 2003; Slagstad et al., 2018; Tomkins et al., 2005). In the two samples from the RIC contact (metasediment and anorthosite sheet), all of the zircon grains show textural evidence for recrystallization and yield a younger observed age range from *c.* 1050 Ma down to *c.* 900 Ma. These data indicate an increase in the degree of resetting closer to the anorthosite complex, where high temperatures persisted, resulting in the youngest apparent ages being recorded at the contact. In addition to the textural evidence for recrystallization, there is also a geochemical trend to lower Th/U ratios among the parts of the original detrital zircons that recorded the youngest ages. This is a well-known (but not universal) characteristic of grains recrystallized during metamorphism (Harley et al., 2007;

Hoskin & Black, 2000; Hoskin & Schaltegger, 2003; Schaltegger et al., 1999) that is related to the expulsion of Th during recrystallization (Harley et al., 2007; Hoskin & Black, 2000).

In long-lived high–*T* scenarios that produce a spread in zircon U–Pb ages as observed here, the prograde–peak–retrograde history may be deciphered by combining both zircon and monazite geochronological data (Clark et al., 2014; Horton, Hacker, Kylander-Clark, Holder, & Jöns, 2016; Johnson, Clark, Taylor, Santosh, & Collins, 2015; Taylor et al., 2016). In this study, a cluster of monazite analyses from the most distal sample ROG13/11 yielded a mean age of 1028 ± 7 Ma, consistent with the equivocal lower intercept of the zircon array in the same sample. This also matches the oldest group of monazite ages recorded by Laurent et al. (2016) and the age of peak regional metamorphism interpreted by Tomkins et al. (2005), Slagstad et al. 2018, and Laurent, Bingen, et al. (2018) based on zircon data. However, this age is older than the *c.* 1000 Ma peak of metamorphism interpreted by Möller et al. (2003) and Drüppel et al. (2013). At the RIC contact, the oldest preserved monazite age was 990 ± 11 Ma (ROG14/5). Monazite at the RIC contact gave the youngest ages, extending down to a minimum of 886 ± 11 Ma (Figure 6c).

Generally, the post-peak path is marked by a transition from predominantly recrystallized original zircon to the appearance of neocrystallised zircon rims which grow when the melt achieves saturation in Zr (Harley et al., 2007; Roberts & Finger, 1997). Hence, we interpret the weighted mean age of zircon rims from the distal sample of 957 ± 15 Ma (Figure 5) as recording the time of regional melt crystallization. This age is consistent with the youngest monazite age (Figure 6) and the 955 ± 8 Ma decompression age reported by Tomkins et al. (2005) from a nearby sample. In contrast, zircon from within the contact aureole show a continuation of ages beyond the interpreted time of regional melt crystallization at *c.* 955 Ma, with no new zircon overgrowths at this time. No distinct metamorphic zircon overgrowths were found in sample ROG13/10 (10km), which likely reflects a more residual bulk composition

during contact metamorphism due to earlier melt loss (Vavra et al., 1996). However, outcrop-scale variations in melt production at this locality are implied by the younger (*c.* 930 Ma) zircon and by epitaxial xenotime ages recorded from the same outcrop reported by Drüppel et al. (2013). In sample ROG13/2 (2 km), three analyses of zircon rims record a weighted mean age of 920 ± 13 Ma that is within uncertainty of the time of emplacement of the RIC (Schärer et al., 1996). At the contact, zircon overgrowths in the anorthosite sheet (ROG14/8) yielded a similar mean age of 917 ± 15 Ma, which overlaps with the youngest ages of recrystallized zircon in paragneiss sample ROG 14/5. As noted above, monazite ages from the latter sample extend even further, down to 886 ± 11 Ma.

By combining the data from multiple geochronometers in a suite of well-constrained samples we can determine the timing of metamorphic events within this complex age continuum. The distal sample records a regional metamorphic event attaining high-*T* at *c.* 1070 Ma and cooling back to the solidus at *c.* 960 Ma, with a proposed peak at *c.* 1030 Ma. Closer to the boundary of the RIC a strong overprint of contact metamorphism associated with anorthosite intrusion at *c.* 930 Ma was followed by melt crystallization at *c.* 920 Ma. The monazite ages suggest that high temperatures persisted until *c.* 890 Ma. Given the continuum of zircon and monazite ages in all samples from within the aureole (ROG13/2, 14/5, 14/8), and the lack of evidence for new zircon growth at *c.* 955 Ma (only recrystallized zircon is present), there is little evidence to suggest that the rocks within the aureole underwent significant cooling in the 100 Myr interval between the regional metamorphic peak (*c.* 1030 Ma) and the emplacement of the RIC (*c.* 930 Ma) (Blereau et al., 2019; Blereau et al., 2017; Laurent, Duchene, et al., 2018) (the *P–T–t* evolution is summarized in Figure 13). We interpret that in the proximity of the RIC, high temperatures were maintained and further elevated throughout this interval, resulting in delayed melt crystallization.

6.3 REE mobility in zircon from the RVA sector

Analyses of the REE concentrations in zircon grains from samples within the RVA Sector show considerable variation in M–HREE abundances and slopes, reflecting changes in temperature that correlate with distance from the RIC (Figure 7). Furthest from the RIC, areas of recrystallized zircon show a larger range of M–HREE concentrations than oscillatory-zoned cores from the same sample, although both preserve positive M–REE slopes. Garnet analyses from the same sample show a complex array of M–HREE patterns (Figure 7e) consistent with prograde subsolidus growth (Grt1 core; melanosome), continued growth in the presence of melt (Grt1 rim; melanosome) and later resorption (Resorbed Grt1; melanosome) (see Hermann and Rubatto (2003) and Rubatto (2002)). However, in samples at the RIC–country rock contact, recrystallized zircon grains have relatively consistent M–HREE slopes that are slightly negative in sample ROG14/5 and steeply positive in sample ROG14/8 (Figure 7c, d). Laser traverses across grains in ROG14/5 show near flat M–HREE profiles and patterns (Figure 14), consistent with the spot analyses (Figure 7g). In both samples the M–HREE signatures are very similar to those of Grt2 in each sample (Figure 7g, h).

The similarities between the REE patterns of primary garnet grains as well as the age and trace element composition of sector zoned zircon found in the anorthosite sheet (ROG14/8) relative to to the host metapelite (ROG14/5) suggests that the garnet and majority of zircon found in sample ROG14/8 were inherited from the metapelite and subsequently recrystallized at high-*T*. The elevated REE abundances in both zircon and garnet in ROG14/8 relative to the metapelite may reflect the simpler mineralogy of the anorthosite in which zircon and garnet were the only HREE sinks, or equilibration with a relatively REE-enriched fluid, although the REE composition of anorthositic melts is poorly constrained and could potentially be relatively enriched.

The variable REE patterns in the zircon and garnet grains are best summarized in a zircon/garnet partitioning array plot (Taylor et al., 2017) in which the Log(D_{Yb}) zircon/garnet partition coefficient is plotted against the M–HREE zircon/garnet partitioning slope: Log(D_{Yb}/D_{Gd}) (Figure 15). On this diagram, analyses of metamorphic zircon in equilibrium with garnet tend to form distinct groups (or linear arrays if variably recrystallised) matching experimentally determined partition coefficients. While those not in equilibrium tend to be scattered and/or plot away from the experimentally-constrained temperature-dependent trend (Taylor et al., 2015). This diagram facilitates the distinction between both original zircon that may not have equilibrated fully with garnet and equilibrated metamorphic zircon, and between different generations of garnet that may be present (Taylor et al., 2017). The relative position of points on the diagram can also be interpreted in terms of temperature of equilibration, although the differences in bulk composition between the rocks under consideration and the experimental study limit the extent to which the equilibration temperature of unknowns can be quantified. Nevertheless, this approach has been particularly useful in interpreting large and/or complex datasets involving recrystallization at high-T (Clark et al., 2018; Guevara et al., 2020; Tucker et al., 2018).

On Figure 14 the REE partitioning data for each zircon analysis is plotted in relation to an average composition of Grt2 from the same sample. The data from recrystallized zircon from sample ROG13/11 form a scattered array of points, at the lower temperature end of the plot, that is partly divergent from the experimental $D_{zrc/grt}$ data trend, suggesting that even far from the contact, zircon underwent some degree of REE equilibration in the presence of garnet. Conversely, at the RIC contact, the REE concentrations of recrystallized zircon in sample ROG14/5 seemingly equilibrated with garnet, with $D_{zrc/grt2}$ values consistent with T>1000°C (Figure 15). Although $D_{zrc/grt}$ values plot around ~1000°C for sample ROG14/8, there is a high

degree of scatter in the data, consistent with the xenocrystic nature of the garnet and majority of the zircon in this sample.

The distribution of metapelitic samples within the array plot is consistent with our diffusion modelling. Sample ROG13/11 plots at a position typical of granulite-facies conditions (Figure 15), and is inferred to have experienced temperatures of ~850–950ºC for *c.* 100 Myr based on independent constraints (Blereau et al., 2019; Blereau et al., 2017; Laurent, Duchene, et al., 2018) (Figure 13). As a result, zircon grains from this sample show minimal trace-element modification (Figure 11a, b). By contrast, sample ROG14/5 shows equilibration between recrystallised zircon and garnet at extreme temperatures (>1000°C; Figure 11e, f) that reflect their close proximity to the anorthosite, and the high intrusion temperature (~1200°C; Westphal et al., 2003).

The M–HREE profiles from traverses across grains within this sample are consistently near 1:1 (Figure 14) and are similar or flatter than the >1000ºC examples shown in Figure 1e, f. Such extreme temperatures match those interpreted based on Ar diffusion profiles in osumilite from sample ROG13/2 (Blereau et al., 2019), but are higher (~150ºC) than estimates based on thermodynamic modelling of samples close to the RIC–country rock contact (specifically sample ROG14/5; Blereau et al., 2017) (Figure 13). This discrepancy most likely reflects the use of the ds6 thermodynamic dataset that does not include osumilite, where osumilite is inferred to have been present within ROG14/5 based on the occurrence of cordierite–K-feldspar–quartz symplectites (Blereau et al., 2017). These higher temperatures are consistent with modelling of osumilite-bearing sample ROG13/2 using the earlier ds5 thermodynamic dataset (Blereau et al., 2019). Alternatively, the temperature discrepancy could indicate that volume diffusion was not the only process acting, and that other processes acted to increase diffusivity, reducing the temperatures required to achieve equilibration and/or indicating longer times at lower temperatures. Under a protracted, more continuous

metamorphic evolution, i.e. where regional and contact metamorphism were not segregated and temperatures remained around 1000ºC for ~150 Myr (i.e. 1070–920 Ma), the REE in zircon would be modified but would require at least 200 Myr at 1000ºC to become fully equilibrated like we see in sample ROG14/5 (Figure 10). Consequently, such a metamorphic evolution with no thermal perturbations would be unlikely to generate the petrological complexities we see, such as secondary generations of garnet and osumilite which characterise the rocks within the aureole. Additionally, this study uses the only available diffusion coefficients for REE in zircon (i.e. Cherniak et al., 1997) and this discrepancy could be a result of the coefficients being inaccurate and overestimating the diffusivities. However, there is no textural evidence that processes other than volume diffusion have operated, the zircon grains themselves are likely to be strongly annealed, and these samples are all highly residual, making a volume diffusion dominated system most probable.

6.4 Implications for the emplacement history of the RIC

U–Pb zircon and baddeleyite geochronology indicates that emplacement of the individual anorthosite bodies in the RIC spanned a duration of <10 Myr (~930–920 Ma) (Schärer et al., 1996), consistent with our diffusion modelling (Figure 10, 11f). However, an Sm–Nd isochron age of 1041 ± 17 Ma for cumulate high-Al orthopyroxene megacrysts from the RIC suggests that the magmatic system may have developed over a much longer timescale (~100 Myr; Bybee et al., 2014), implying a significant time lag between the initial development and differentiation of the magmatic system in the deep crust and final emplacement of the anorthosite. The RIC contains three anorthosite plutons and a layered complex with crystallisation ages that are within uncertainty of each other, consistent with up to five pulses of magmatism (Bolle, Trindade, Bouchez, & Duchesne, 2002; Charlier et al., 2010). Previous 2–D thermal modelling undertaken by Westphal et al. (2003) to explain the spatial distribution

of the high-*T* mineral isograds adjacent to the anorthosite intrusion suggested an initial pulse of magmatism to raise the country rock temperatures, followed by emplacement 3 Myr later of a smaller hotter intrusion over the next 2 Myr. A temperature of ~1100°C was only achieved in the country rocks close to the second intrusion and was only maintained for <1 Myr (Westphal et al., 2003). However, their modelling used a starting country rock temperature of 600°C; ~200°C colder than the minimum regional metamorphic temperatures (Blereau et al., 2019; Blereau et al., 2017; Laurent, Duchene, et al., 2018). While the interpretation of how the contact metamorphic event affected the region has changed (Coint et al., 2015, Blereau et al., 2019), a similar multiple pulse approach to Westphal et al. (2003) was still worth investigating to account for the multiple plutons within the RIC. An initial country rock temperature of ≥800°C would have reduced time required to reach the maximum country rock temperatures in the model (5 Myr to reach 1100°C). As the frequency and duration of magmatic pulses have had a strong influence on the size and thermal gradient of the aureole (Cao, Kaus, & Paterson, 2016), we conducted 2–D thermal modelling of different emplacement scenarios for comparison with the *T–t* paths indicated by our REE data. 2–D thermal models with magmatic pulses every 1 and 2 Myrs (Figure 16a, b) resulted in only a ~200°C increase in the temperature of the country rocks within the aureole, requiring an overall emplacement time of at least 2 Myr (similar to Westphal et al., 2003), with the resulting temperatures being insufficient to replicate our REE data.

A growing number of studies propose that plutons are constructed incrementally as numerous small pulses over tens of thousands to millions of years as opposed to more traditional larger discrete bodies, which is particularly important for the emplacement of crystal-rich mushes (Coleman, Gray & Glazner, 2004; Farina, Stevens & Villaros, 2012; Miller et al., 2011). While there is a magmatic fabric in portions of the anorthosite, including the Egersund-Ogna pluton (e.g. Charlier et al., 2010), incremental emplacement correlates with the

short interval of time over which such fabrics can form prior to crystallisation (e.g. Paterson et al., 1998). Modelling of an incremental emplacement scenario of multiple pulses of magma every *c.* 10,000 years (Figure 16c) predicts a temperature of ~1100°C in the immediately adjacent country rock that would be maintained for as long as the introduction of material continued and that is sufficiently high to lead to reequilibration of REE in zircon within *c.* 170,000 years. This rapid, multiple-pulse model is the simplest geodynamic scenario that satisfies observations (Figure 15c), and is our preferred scenario for emplacement of the RIC.

7. CONCLUSIONS

- Under extreme conditions for crustal rocks (≥1000°C), (pure volume) diffusion profiles of REE in zircon are applicable as a thermometer and speedometer for high temperature processes.
- Zircon grains experiencing lower temperatures of metamorphism (<900°C) will largely retain their original REE compositions, even when those elevated temperatures are long lived (≥100 Myr).
- New zircon and monazite U–Pb geochronology for the RVA Sector, Norway, supports peak regional metamorphism at 1028 ± 7 Ma, consistent with previous studies. Zircon rims associated with post-peak regional melt crystallization developed in migmatites outside the RIC aureole by 957 ± 15 Ma. No further zircon or monazite growth was found beyond this age in samples >10km from the RIC, based on this and previous studies.
- Samples within the RIC aureole show a continuum of zircon and monazite U–Pb ages rather than two discrete age events, with no clear melt crystallization event until after the emplacement of the RIC (*c.* 920 Ma). This is explained by prolonged residence

under high-temperature conditions associated with a slow cooling rate following regional metamorphism and proximity to a long-lived magmatic system.

- Results of REE in zircon diffusion modelling indicate emplacement of the RIC incrementally over 1–5 Myr, which would have caused significantly elevated temperatures at the contact (~1100°C) but minimal thermal effects on rocks at greater distance (<1000°C at 2km, <800°C at 10km).

ACKNOWLEDGEMENTS

Financial support for this project was provided by an ARC DECRA fellowship (DE120103067) to CC. EB was supported by an Australian Government Research Training Program Scholarship. The custom python code used to calculate the theoretical profiles for REE diffusion within zircon has been made available as an interactive Jupyter notebook on the following Github repository: https://github.com/es1208/REE_concentrations_in_zircon.

We thank D. Viete and T. Slagstad, B. Bingen and A. Kylander-Clark for their comments on an earlier version of this paper, and Trond Slagstad and an anonymous reviewer for their constructive reviews of this version. The authors have no conflicts of interest to declare.

REFERENCES

Ashwal, L. D., & Bybee, G. M. (2017). Crustal evolution and the temporality of anorthosites. *Earth-Science Reviews, 173*, 307-330.

Bergh, S. G., Corfu, F., Myhre, P. I., Kullerud, K., Armitage, P. E., Zwaan, K. B., ... & Chattopadhya, A. (2012). Was the Precambrian basement of Western Troms and Lofoten-Vesterålen in northern Norway linked to the Lewisian of Scotland? A comparison of crustal components, tectonic evolution and amalgamation history. *Tectonics–Recent Advances. InTech, Rijeka*, 283-330.

Bhattacharya, S., & Kar, R. (2002). High-temperature dehydration melting and decompressive P–T path in a granulite complex from the Eastern Ghats, India. *Contributions to Mineralogy and Petrology, 143*(2), 175-191.

Bingen, B., Davis, W. J., Hamilton, M. A., Engvik, A. K., Stein, H. J., Skår, Ø., & Nordgulen, Ø. (2008). Geochronology of high-grade metamorphism in the Sveconorwegian belt, S. Norway: U–Pb, Th–Pb and Re–Os data. *Norwegian Journal of Geology, 88*, 13-42.

Bingen, B., Viola, G., Möller, C., Auwera, J. V., Laurent, A., & Yi, K. (2020). The Sveconorwegian orogeny. *Gondwana Research*. https://doi.org/10.1016/j.gr.2020.10.014

Blereau, E., Clark, C., Jourdan, F., Johnson, T. E., Taylor, R. J. M., Kinny, P. D., . . . Eroglu, E. (2019). Closed system behaviour of argon in osumilite records protracted high-temperature metamorphism within the Rogaland-Vest Agder Sector, Norway. *Journal of Metamorphic Geology, 37*(5), 667-680.

Blereau, E., Johnson, T. E., Clark, C., Taylor, R. J. M., Kinny, P. D., & Hand, M. (2017). Reappraising the P–T evolution of the Rogaland–Vest Agder Sector, southwestern Norway. *Geoscience Frontiers, 8*(1), 1-14.

Bolle, O., Diot, H., Liégeois, J. P., & Vander Auwera, J. (2010). The Farsund intrusion (SW Norway): a marker of Late-Sveconorwegian (Grenvillian) coeval transtension and gravity-driven tectonism. *Journal of Structural Geology*, *32*, 1500-1518.

Bolle, O., Trindade, R. I. F., Bouches, J. L., & Duchesne, J.-C. (2002). Imaging downward granitic transport in the Rogaland Igneous Complex, SW Norway. *Terra Nova*, 14, 87-92.

Bybee, G. M., Ashwal, L. D., Shirey, S. B., Horan, M., Mock, T., & Andersen, T. B. (2014). Pyroxene megacrysts in Proterozoic anorthosites: Implications for tectonic setting,

magmaa source and magmatic processes at the Moho. *Earth and Planetary Science Letters, 389*, 74-85.

Cao, W., Kaus, B. J. P., & Paterson, S. (2016). Intrusion of granitic magma into the continental crust facilitated by magma pulsing and dike-diapir interactions: Numerical simulations. *Tectonics, 35*(6), 1575-1594.

Charlier, B., Duchesne, J. C., Vander Auwera, J., Storme, J. Y., Maquil, R., & Longhi, J. (2010). Polybaric fractional crystallization of high-alumina basalt parental magmas in the Egersund–Ogna massif-type anorthosite (Rogaland, SW Norway) constrained by plagioclase and high-alumina orthopyroxene megacrysts. *Journal of Petrology*, 51(12), 2515-2546.

Cherniak, D. J., Hanchar, J. M., & Watson, E. B. (1997). Rare-earth diffusion in zircon. *Chemical Geology, 134*(4), 289-301.

Cherniak, D. J., & Watson, E. B. (2001). Pb diffusion in zircon. *Chemical Geology, 172*(1–2), 5-24.

Cherniak, D. J., & Watson, E. B. (2003). Diffusion in zircon. *Reviews in Mineralogy and Geochemistry, 53*(1), 113-143.

Clark, C., Healy, D., Johnson, T., Collins, A. S., Taylor, R., Santosh, M., & Timms, N. E. (2015). Hot orogens and supercontinent amalgamation: A Gondwanan example from southern India. *Gondwana Research, 28*(4), 1310-1328.

Clark, C., Kirkland, C. L., Spaggiari, C. V., Oorschot, C., Wingate, M. T. D., & Taylor, R. J. (2014). Proterozoic granulite formation driven by mafic magmatism: An example from the Fraser Range Metamorphics, Western Australia. *Precambrian Research, 240*, 1-21.

Clark, C., Taylor, R. J. M., Kylander-Clark, A. R. C., & Hacker, Bradley R. (2018). Prolonged (>100 Ma) ultrahigh temperature metamorphism in the Napier Complex, East

Antarctica: A petrochronological investigation of Earth's hottest crust. *Journal of Metamorphic Geology, 36*(9), 1117-1139.

Coint, N., Slagstad, T., Roberts, N. M. W., Marker, M., Røhr, T. S., & Sørensen, B. E. (2015). The Late Mesoproterozoic Sirdal Magmatic Belt, SW Norway: Relationships between magmatism and metamorphism and implications for Sveconorwegian orogenesis. *Precambrian Research, 265*, 57-77.

Coleman, D. S., Gray, W., & Glazner, A. F. (2004). Rethinking the emplacement and evolution of zoned plutons: Geochronologic evidence for incremental assembly of the Tuolumne Intrusive Suite, California. *Geology*, 32(5), 433-436

Crank, J. (1975). The Mathematics of Diffusion: 2d Ed.: Oxford University Press.

Degeling, H., Eggins, S., & Ellis, D. J. (2001). Zr budgets for metamorphic reactions, and the formation of zircon from garnet breakdown. *Mineralogical Magazine, 65*(6), 749-758.

Drüppel, K., Elsäßer, L., Brandt, S., & Gerdes, A. (2013). Sveconorwegian Mid-crustal Ultrahigh-temperature Metamorphism in Rogaland, Norway: U-Pb LA-ICP-MS Geochronology and Pseudosections of Sapphrine Granulites and Associated Paragneisses. *Journal of Petrology, 54*(2), 305-350.

Ellis, D. J., Sheraton, J. W., England, R. N., & Dallwitz, W. B. (1980). Osumilite-sapphirine-quartz granulites from Enderby Land Antarctica - mineral assemblages and reactions. *Contributions to Mineralogy and Petrology, 72*, 123-143.

Farina, F., Stevens, G., & Villaros, A. (2012). Multi-batch, incremental assembly of a dynamic magma chamber: the case of the Peninsula pluton granite (Cape Granite Suite, South Africa). *Mineralogy and Petrology*, 106(3-4), 193-216.

Guevara, V. E., MacLennan, S. A., Dragovic, B., Caddick, M. J., Schoene, B., Kylander-Clark, A. R., & Couëslan, C. G. (2020). Polyphase zircon growth during slow cooling

from ultrahigh temperature: an example from the Archean Pikwitonei Granulite Domain. *Journal of Petrology*.

Halpin, J. A., Daczko, N. R., Milan, L. A., & Clarke, G. L. (2012). Decoding near-concordant U–Pb zircon ages spanning several hundred million years: recrystallisation, metamictisation or diffusion? *Contrib Mineral Petrol, 163*(1), 67-85.

Harley, S. L. (2016). A matter of time: The importance of the duration of UHT metamorphism. *Journal of Mineralogical and Petrological Sciences, 111*, 50–72.

Harley, S. L., Kelly, N. M., & Möller, A. (2007). Zircon behaviour and the thermal histories of mountain chains. *Elements, 3*, 25-30.

Hermann, J., & Rubatto, D. (2003). Relating zircon and monazite domains to garnet growth zones: age and duration of granulite facies metamorphism in the Val Malenco lower crust. *Journal of Metamorphic Geology, 21*, 833-852.

Hokada, T., & Harley, S. L. (2004). Zircon growth in UHT leucosome: ocnstraints from zircon-garnet rare earth elements (REE) relations in Napier Complex, East Antarctica. *Journal of Mineralogical and Petrological Sciences,* **99**, 180-190.

Holder, R. M., Hacker, B. R., Horton, F., & Rakotondrazafy, A. F. M. (2018). Ultrahigh-temperature osumilite gneisses in southern Madagascar record combined heat advection and high rates of radiogenic heat production in a long-lived high-T orogen. *Journal of Metamorphic Geology, 36*(7), 855-880.

Horton, F., Hacker, B., Kylander-Clark, A., Holder, R., & Jöns, N. (2016). Focused radiogenic heating of middle crust caused ultrahigh temperatures in southern Madagascar. *Tectonics, 35*(2), 293-314.

Hoskin, P. W. O., & Black, L. P. (2000). Metamorphic zircon formation by solid-state recrystallization of protolith igneous zircon. *Journal of Metamorphic Geology, 18*, 423-439.

Hoskin, P. W. O., & Schaltegger, U. (2003). The composition of zircon and igneous and metamorphic petrogenesis. In J. M. Hanchar, P. W. O. Hoskin, P. H. Ribbe, J. J. Rosso, P. H. Ribbe, & J. J. Rosso (Eds.), *Zircon*.

Jansen, B. H., Blok, R. J. P., Bos, M., & Scheelings, M. (1985). Geothermometry and geobarometry in Rogaland and preliminary results from the Bamble area, S Norway. *The Deep Proterozoic Crust in the North Atlantic Provinces*, 499-516.

Johnson, T., Clark, C., Taylor, R., Santosh, M., & Collins, A. S. (2015). Prograde and retrograde growth of monazite in migmatites: An example from the Nagercoil Block, southern India. *Geoscience Frontiers, 6*(3), 373-387.

Kelly, N. M., & Harley, S. L. (2005). An integrated microtextural and chemical approach to zircon geochronology: refining the Archaean history of the Napier Complex, east Antartica. *Contributions to Mineralogy and Petrology, 149*, 57-84.

Kelly, N. M., Harley, S. L., & Möller, A. (2012). Complexity in the behavior and recrystallization of monazite during high-T metamorphism and fluid infiltration. *Chemical Geology, 322-323*, 192-208.

Kelsey, D. E. (2008). On ultrahigh-temperature crustal metamorphism. *Gondwana Research, 13*, 1-29.

Korhonen, F. J., Brown, M., Clark, C., & Bhattacharya, S. (2013a). Osumilite-melt interactions in the ultrahigh temperatures granulites: phase equilibria modelling and implications for the P-T-t evolution of the Eastern Ghats Provincee, India. *Journal of Metamorphic Geology, 31*, 881-907.

Korhonen, F. J., Clark, C., Brown, M., Bhattacharya, S., & Taylor, R. (2013b). How long-lived is ultrahigh temperature (UHT) metamorphism? Constraints from zircon and monazite geochronology in the Eastern Ghats orogenic belt, India. *Precambrian Research*, *234*, 322-350.

Kusiak, M. A., Dunkley, D. J., Wirth, R., Whitehouse, M. J., Wilde, S. A., & Marquardt, K. (2015). Metallic lead nanospheres discovered in ancient zircons. *Proceedings of the National Academy of Sciences, 112*(16), 4958-4963.

Kusiak, M. A., Whitehouse, M. J., Wilde, S. A., Nemchin, A. A., & Clark, C. (2013). Mobilization of radiogenic Pb in zircon revealed by ion imaging: Implications for early Earth geochronology. *Geology, 41*(3), 291-294.

Laurent, A. T., Bingen, B., Duchene, S., Whitehouse, M. J., Seydoux-Guillaume, A.-m., & Bosse, V. (2018). Decoding a protracted zircon geochronological record in ultrahigh temperature granulite, and persistence of partial melting in the crust, Rogaland, Norway. *Contributions to Mineralogy and Petrology, 173*(4), 29.

Laurent, A. T., Duchene, S., Bingen, B., Bosse, V., & Seydoux-Guillaume, A.-M. (2018). Two successive phases of ultrahigh temperature metamorphism in Rogaland, S. Norway: evidence from Y-in-monazite thermometry. *Journal of Metamorphic Geology, 36*(8), 1009-1037.

Laurent, A. T., Seydoux-Guillaume, A.-M., Duchene, S., Bingen, B., Bosse, V., & Datas, L. (2016). Sulphate incorporation in monazite lattice and dating the cycle of sulphur in metamorphic belts. *Contributions to Mineralogy and Petrology, 171*(11), 94.

Lee, J. K. W., Williams, I. S., & Ellis, D. J. (1997). Pb, U and Th diffusion in natural zircon. *Nature, 390*(6656), 159-162.

Maijer, C. (1987). The metamorphic envelope of the Rogaland intrusive complex. *Norges Geologisk Undersøkelse- Special Publication, 1*, 68-73.

Marker, M., Schiellerup, H., Meyer, G., Robins, B., & Bolle, O. (2003). Introduction to the geological map of the Rogaland Anorthosite Province 1:75000. *Norges Geologisk Undersøkelse- Special Publication, 9*, 109-116.

Miller, C. F., Furbish, D. J., Walker, B. A., Claiborne, L. L., Koteas, G. C., Bleick, H. A., & Miller, J. S. (2011). Growth of plutons by incremental emplacement of sheets in crystal-rich host: Evidence from Miocene intrusions of the Colorado River region, Nevada, USA. *Tectonophysics*, 500(1-4), 65-77.

Möller, A., O'Brien, P. J., Kennedy, A., & Kröner, A. (2002). Polyphase zircon in ultrahigh-temperature granulites (Rogaland, SW Norway): constraints for Pb diffusion in zircon. *Journal of Metamorphic Geology, 20*, 727-740.

Möller, A., O'Brien, P. J., Kennedy, A., & Kröner, A. (2003). Linking growth episodes of zircon and metamorphic textures to zircon chemistry: an example from the ultrahigh-temperature granulites of Rogaland (SW Norway). *Geological Society, London, Special Publications, 220*(From: Vance, D., Müller, W., & Villa, I. M. (eds) 2003. Geochronology: Linking the Isotopic Record with Petrology and Textures.), 65-81.

Nasdala, L., Lengauer, C. L., Hanchar, J. M., Kronz, A., Wirth, R., Blanc, P., ... & Seydoux-Guillaume, A. M. (2002). Annealing radiation damage and the recovery of cathodoluminescence. *Chemical Geology*, 191(1-3), 121-140.

Pasteels, P., Demaiffe, D., & Michot, J. (1979). U–Pb and Rb–Sr geochronology of the eastern part of the south Rogaland igneous complex, southern Norway. *Lithos, 12*, 199-208.

Paterson, S. R., Fowler Jr., T. K., Schmidt, K. L., Yoshinobu, A. S., Yuan, E. S., & Miller, R. B. (1998). Interpreting magmatic fabirc patterns in plutons. *Lithos*, *44*(1-2), 53-82.

Peterman, E. M., Reddy, S. M., Saxey, D. W., Snoeyenbos, D. R., Rickard, W. D. A., Fougerouse, D., & Kylander-Clark, A. R. C. (2016). Nanogeochronology of discordant zircon measured by atom probe microscopy of Pb-enriched dislocation loops. *Science Advances, 2*(9).

Roberts, M. P., & Finger, F. (1997). Do U-Pb zircon ages from granulites reflect peak metamorphic conditions?. *Geology*, *25*(4), 319-322.

Roberts, N. M. W., & Slagstad, T. (2015). Continental growth and reworking on the edge of the Columbia and Rodinia supercontinents; 1.86–0.9 Ga accretionary orogeny in southwest Fennoscandia. *International Geology Review, 57*(11-12), 1582-1606.

Rubatto, D. (2002). Zircon trace element geochemistry: partitioning with garnet and the link between U-Pb ages and metamorphism. *Chemical Geology, 184*.

Rubatto, D. (2017). Zircon: The Metamorphic Mineral. *Reviews in Mineralogy and Geochemistry, 83*(1), 261.

Rubatto, D., & Hermann, J. (2007). Experimental zircon/melt and zircon/garnet trace element partitioning and implications for the geochronology of crustal rocks. *Chemical Geology, 241*, 38-61.

Schaltegger, U., Fanning, C. M., Günther, D., Maurin, J. C., Schulmann, K., & Gebauer, D. (1999). Growth, annealing and recrystallization of zircon and preservation of monazite in high-grade metamorphism: conventional and in-situ U-Pb isotope, cathodoluminesecence and microchemical evidence. *Contributions to Mineralogy and Petrology, 134*, 186-201.

Schärer, U., Wilmart, E., & Duchesne, J-C. (1996). The short duration and anorogenic character of anorthosite magmatism: U–Pb dating of the Rogaland complex, Norway. *Earth and Planetary Science Letters, 139*, 335-350.

Slagstad, T., Marker, M., Roberts, N. M., Saalmann, K., Kirkland, C. L., Kulakov, E., ... & Sørensen, B. E. (2020). The Sveconorwegian orogeny–Reamalgamation of the fragmented southwestern margin of Fennoscandia. *Precambrian Research*, 350, 105877.

Slagstad, T., Roberts, N. M. W., Coint, N., Høy, I., Sauer, S., Kirkland, C. L., . . . Bybee, G. M. (2018). Magma-driven, high-grade metamorphism in the Sveconorwegian Province,

southwest Norway, during the terminal stages of Fennoscandian Shield evolution. *Geosphere, 14*(2), 861-882.

Slagstad, T., Roberts, N. M. W., & Kulakov, E. (2017). Linking orogenesis across a supercontinent; the Grenvillian and Sveconorwegian margins on Rodinia. *Gondwana Research, 44*, 109-115.

Slagstad, T., Roberts, N. M. W., Marker, M., Røhr, T. S., & Schiellerup, H. (2013). A non-collisional, accretionary Sveconorwegian orogen. *Terra Nova, 25*, 30-37.

Spencer, C. J., Kirkland, C. L., & Taylor, R. J. M. (2016). Strategies towards statistically robust interpretations of in situ U–Pb zircon geochronology. *Geoscience Frontiers, 7*(4), 581-589.

Spencer, C. J., Roberts, N. M. W., Cawood, P. A., Hawkesworth, C. J., Prave, A. R., Antonini, A. S. M., . . . EIMF. (2014). Intermontane basins and bimodal volcanism at the onset of the Sveconorwegian Orogeny, southern Norway. *Precambrian Research, 252*, 107-118.

Taylor, R., Clark, C., Fitzsimons, I. C. W., Santosh, M., Hand, M., Evans, N., & McDonald, B. (2014). Post-peak, fluid-mediated modification of granulite facies zircon and monazite in the Trivandrum Block, southern India. *Contrib Mineral Petrol, 168*(2), 1-17.

Taylor, R., Harley, S. L., Hinton, R. W., Elphick, S., Clark, C., & Kelly, N. M. (2015). Experimental determination of REE partition coefficients between zircon, garnet and melt: a key to understanding high-T crustal processes. *Journal of Metamorphic Geology, 33*, 231–248.

Taylor, R. J. M., Clark, C., Harley, S. L., Kylander-Clark, A. R. C., Hacker, B. R., & Kinny, P. D. (2017). Interpreting granulite facies events through rare earth element partitioning arrays. *Journal of Metamorphic Geology*, 1-17.

Taylor, R. J. M., Kirkland, C. L., & Clark, C. (2016). Accessories after the facts: Constraining the timing, duration and conditions of high-temperature metamorphic processes. *Lithos, 264*, 239-257.

Taylor, R. J., Johnson, T. E., Clark, C., & Harrison, R. J. (2020). Persistence of melt-bearing Archean lower crust for> 200 my—an example from the Lewisian Complex, northwest Scotland. Geology, 48(3), 221-225.

Tobi, A. C., Hermans, G. A. E. M., Maijer, C., & Jansen, B. H. (1985). Metamorphic zoning in the high-grade Proterozoic of Rogaland-Vest Agder, SW Norway. *The Deep Proterozoic Crust in the North Atlantic Provinces*, 477-497.

Tomkins, H. S., Williams, I. S., & Ellis, D. J. (2005). In situ U–Pb dating of zircon formed from retrograde garnet breakdown during decompression in Rogaland, SW Norway. *Journal of Metamorphic Geology, 23*, 201-215.

Tucker, N. M., Hand, M., Kelsey, D. E., Taylor, R., Clark, C., & Payne, J. L. (2018). A tripartite approach to unearthing the duration of high temperature conditions versus peak metamorphism: An example from the Bunger Hills, East Antarctica. *Precambrian Research, 314*, 194-220.

Vavra, G., Gebauer, D., Schmid, R., & Compston, W. (1996). Multiple zircon growth and recrystallization during polyphase Late Carboniferous to Triassic metamorphism in granulites of the Ivrea Zone (Southern Alps): an ion microprobe (SHRIMP) study. *Contributions to Mineralogy and Petrology, 122*, 337-358.

Verschure, R. H., Andriessen, P. A. M., Boelrijk, N. A. I. M., Hebeda, E. H., Maier, W. D., Priem, H. N. A., & Verdurmen, E. A. T. (1980). On the thermal stability of Rb–Sr and K–Ar biotite systems: evidence from coexisting Sveconorwegian (ca 870 Ma) and Caledonian (ca 400 Ma) biotites in SW Norway. *Contributions to Mineralogy and Petrology, 74*, 245-252.

Westphal, M., Schumacher, J. C., & Boschert, S. (2003). High-Temperature Metamorphism and the Role of Magmatic Heat Sources at the Rogaland Anorthosite Complex in Southwestern Norway. *Journal of Petrology, 44*(6), 1145-1162.

White, R. W., Powell, R., Holland, T. J. B., Johnson, T., & Green, E. C. R. (2014). New mineral activity-composition relations for thermodynamic calculations in metapelitic systems. *Journal of Metamorphic Geology, 32*, 261-286.

Whitehouse, M. J., Kusiak, M. A., Wirth, R., & Ravindra Kumar, G. R. (2017). Metallic Pb nanospheres in ultra-high temperature metamorphosed zircon from southern India. *Mineralogy and Petrology, 111*(4), 467-474.

Wohletz, K., Civetta, L., & Orsi, G. (1999). Thermal evolution of the Phlegraean magmatic system. *Journal of Volcanology and Geothermal Research, 91*(2–4), 381-414.

Table 1: Summary of metamorphic U–Pb geochronology from gneisses surrounding the Rogaland Igneous Complex

Lithology	Technique	Accessory mineral	U–Pb Age (206/238) *(207/206)	Description	Aureole Y/N	Reference
Ortho/ paragneisses	SIMS	Zircon	c. 1050 Ma	Magmatic cores	Y	Möller et al., 2003
			*1037 ± 11 Ma	Magmatic cores		
			*1015 ± 11 Ma	Metamorphic zircons (recrystallised + featureless overgrowths)		
			927 ± 7 Ma	Metamorphic rims		
			908 ± 9 Ma	Metamorphic rims, low Th/U		
Paragneiss	SIMS	Zircon	*3.05 ± 67 – 1.34 ± 77 Ga	Detrital zircon	N	Tomkins et al., 2005
			1037 ± 10 – 973 ± 13 Ma	Recrystallised zircon		
			1035 ± 9 Ma	Metamorphic zircon		
			955 ± 8 Ma	Metamorphic zircon in cordierite		
Paragneiss	LA-ICP-MS	Zircon	*1064 ± 38 – 989 ± 49 Ma	Metamorphic rims	Y	Drüppel et al., 2013
			*1029 ± 32 – 993 ± 23 Ma	Metamorphic zircon		
		Zircon and Xenotime	*1006 ± 4 Ma	Zircon rims and xenotime		
		Xenotime	*c. 1001–979 Ma	Single grains		
			*933 ± 5 Ma	Epitaxial		
			*928 ± 10 Ma	Epitaxial		
Paragneiss	LA-ICP-MS	Monazite	1034 ± 6 Ma	Sulphate-rich cores	Y	Laurent et al., 2016
			1005 ± 7 Ma	Secondary sulphate-bearing domains		
			935 ± 7 Ma	S-free Y -rich domains		

Paragneisses	SIMS	Zircon	1028 ± 7 Ma	CL-dark rims	N	Laurent, Bingen et al., 2018
			1039 ± 28 to 955 ± 17 Ma	CL-dark rims and dark sector-zoned zircon		
			1503 ± 9 and 1024 ± 18 Ma	Low-U cores and CL-dark margin respectively	Y	
			1014 ± 25 to 951 ± 22 Ma; 942 ± 8 Ma	CL-dark rims and inner CL-grey domain respectively		
			1030 ± 20 to 936 ± 18; 940 ± 12 Ma	CL-dark rims and CL-dark sector zoned respectively		
Orthogneisses	SIMS/LA-ICP-MS	Zircon	1277 ± 23 Ma	Rim 1	N	Slagstad et al., 2018
			1014 ± 14 Ma	Rim 2		
Paragneiss			1025 ± 10 Ma	Metamorphic rims		
			1027 ± 6 Ma	Metamorphic rims		
Orthogneisses			1031 ± 5 Ma	Rims and cores		
			1039 ± 24 Ma	Metamorphic rims		
Paragneiss			1043 ± 8 Ma	Migmatisation		
			1049 ± 19 Ma	Metamorphic rims		
Orthogneisses			1065 ± 23 Ma	Metamorphic rims		
			1080–920 Ma	Metamorphic zircon		
			1080–920 Ma	Metamorphic zircon		
			1130–950 Ma	Metamorphic zircon		
Paragneisses			1050–940 Ma	Metamorphic zircon	Y	
			1060–960 Ma	Metamorphic zircon		
			938 ± 6 Ma	Metamorphic zircon		
Paragneiss (30km)	SIMS	Zircon	1917 ± 6 – 1158 ± 99 Ma*	Detrital cores	N	This study
			1292 ± 14 – 1009 ± 15 Ma	Recrystallised zircon		
			957 ± 15 Ma	Metamorphic rims		

Paragneiss (10 km)		Monazite	1038 ± 11 – 960 ± 11 Ma	Range of monazite dates		
			1028 ± 7 Ma	Weighted mean monazite age		
		Zircon	1549 ± 19 – 1376 ± 7 Ma*	Detrital cores		
			1502 ± 19 – 1055 ± 13 Ma	Recrystallised zircon		
Paragneiss (2 km)		Zircon	1574 ± 27 – 1011 ± 18 Ma	Oscilatory zoned cores and recrystallised areas		
			920 ± 13 Ma	Metamorphic rims		
			899 ± 15 Ma	Sector zoned zircon		
Paragneiss (~10 m)		Monazite	1037 ± 11 – 983 ± 12 Ma	Range of monazite dates	Y	
		Zircon	1025 ± 15 – 919 ± 18 Ma	Recrystallised and sector zoned zircon		
		Monazite	990 ± 11 – 886 ± 11 Ma	Range of monazite dates		
Grt-bearing anorthosite (~10 m)		Zircon	1045 ± 17 – 1036 ± 11 Ma	Unzoned cores		
			1017 ± 11 – 926 ± 12 Ma	Recrystallised zircon		
			917 ± 12 Ma	Overgrowth rims		

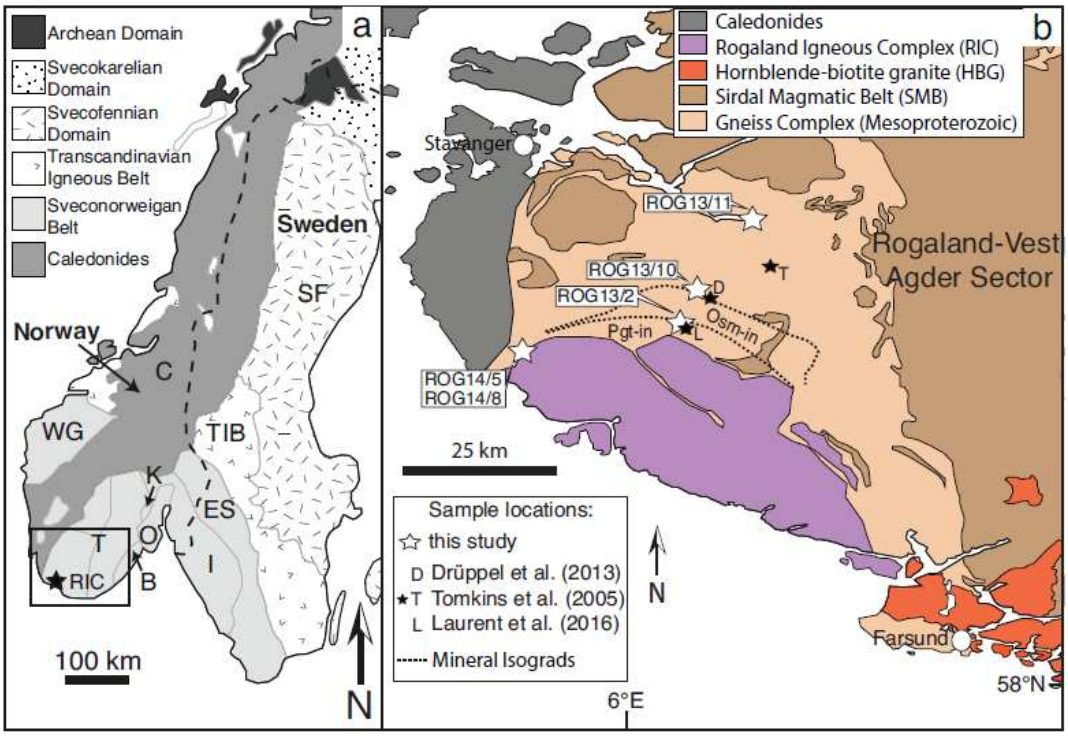

Figure 1: (a) - Map showing the main geological domains of Scandinavia (after Bergh et al., 2012). Abbreviations: T – Telemarkia Terrane; B – Bamble Sector; O – Oslo Graben; K – Kongsberg Sector; I – Idefjorden Terrane; ES – Eastern Segment; C – Caledonides; TIB – Transcandinavian Igneous Belt; SF – Svecofennian Foreland; WG – Western Gneiss Region. (b) Geological map of the Rogaland-Vest Agder Sector (after Coint et al., 2015, mineral isograds from Bolle, Diot, Liégeois, & Auwera, 2010). Samples from this study are marked as white stars with locations from previous studies marked as smaller black stars. See online version for colour.

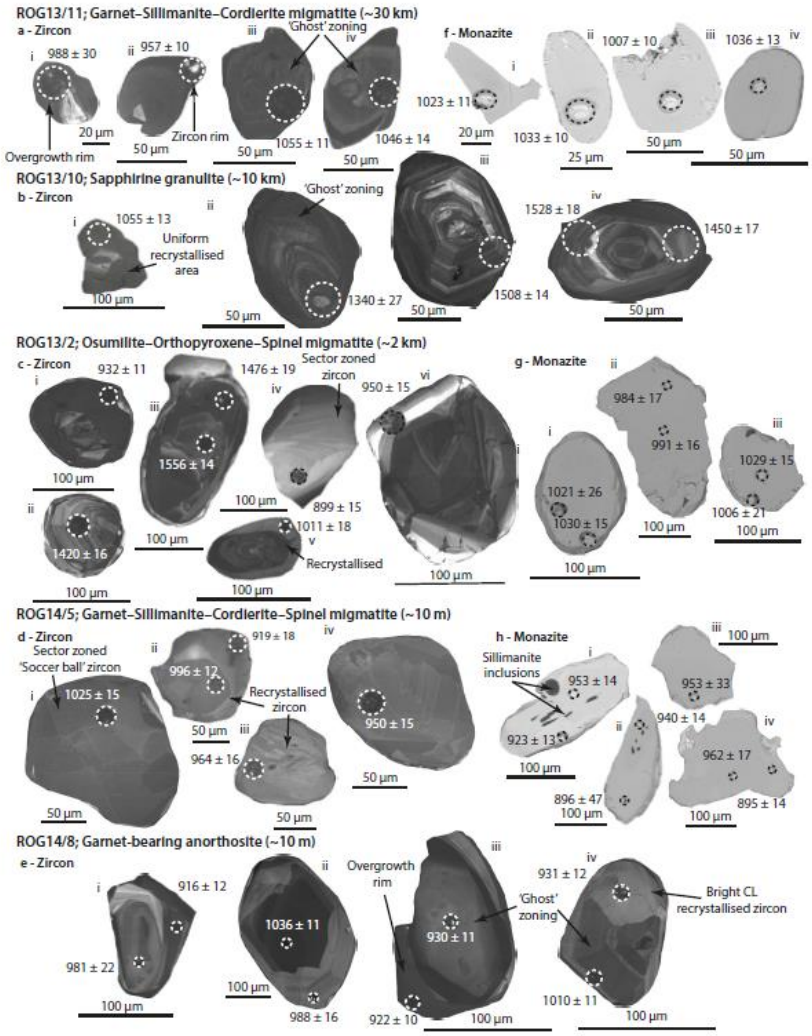

Figure 2: Representative zircon and monazite grains imaged using CL (zircon) and BSE imaging (monazite). Marked spots are LA–ICP–MS spots placed over SHRIMP spots, except for ROG13/10 (SHRIMP spots only). (a) - Zircons from ROG13/11. (i, iv) Grains with bright CL response cores and dark uniform overgrowths. (ii-iv) Recrystallized zircons with convoluted to diffuse ghost zoning. (b) - Zircons from ROG13/10. (i) Bright CL response core with dark uniform recrystallized zircon. (ii) Recrystallized zircon with diffuse oscillatory zoning. (iii–iv) Inherited cores with oscillatory zoning. (c) - Zircon from ROG13/2. (i) Recrystallized oscillatory zoned core with dark overgrowth. (ii) Bright oscillatory zoned inherited core. (iii) Dark inherited core with darker recrystallised regions containing minor ghost zoning. (iv) Bright CL response sector zoned grain. (v-vi) Recrystallized cores with bright CL response overgrowths. (d) - Zircon from ROG14/5. (i, iv) Sector zoned zircon. (ii, iii). Recrystallized zircon with convoluted zoning. (e) - Zircon from ROG14/8. (i-iii) Recrystallized zircon with diffused zoning and dark overgrowths. (ii, iv) recrystallized zircon with bright CL response regions. (f) - Monazite from ROG13/11. (i-iv) uniform BSE response monazite. (g) - Monazite from ROG13/2. (i-iii) uniform BSE response monazite. h- Monazite from ROG14/5. (i, ii) Monazite with dark BSE response core with sillimanite inclusions and bright BSE response outer region. (iii, iv) Inclusion free monazite with limited variation in BSE response.

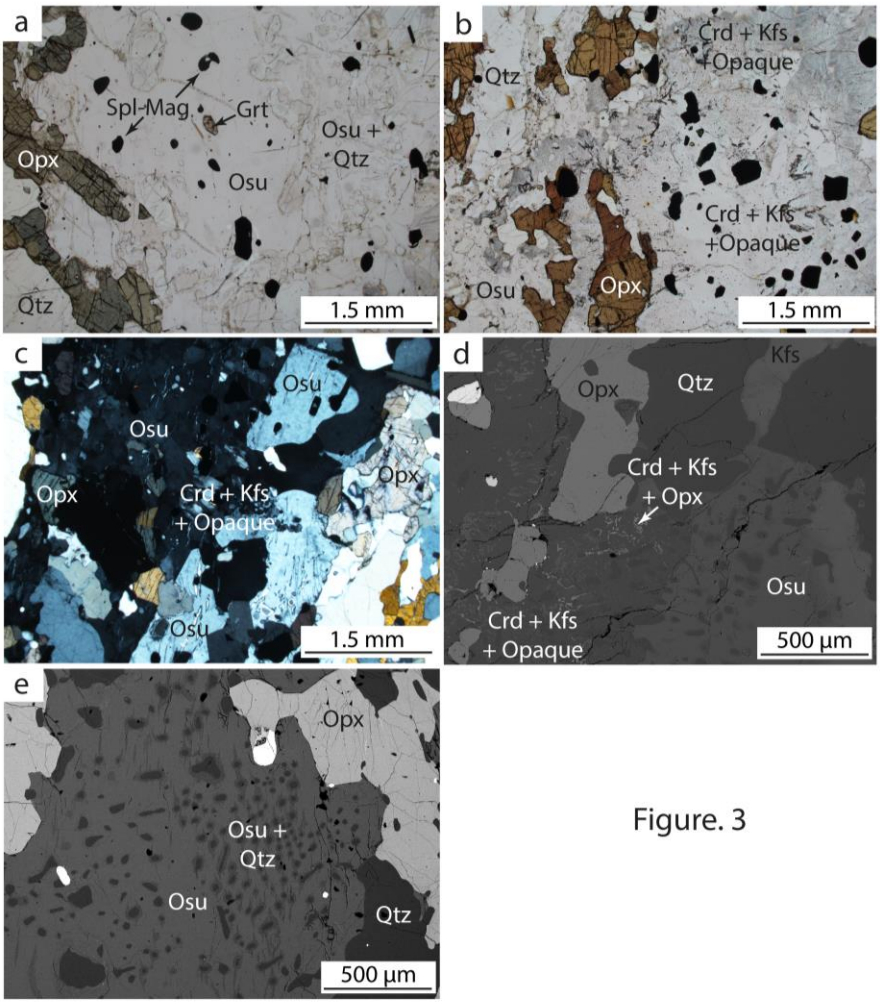

Figure. 3

Figure 3: Photomicrographs and BSE images of ROG13/2, an osumilite–orthopyroxene–spinel migmatite. (a) - PPL photomicrograph of a large osumilite grain with inclusions of spinel/magnetite and garnet, bounded by an osumilite–quartz intergrowth. (b) - PPL photomicrograph of a cordierite–K-feldspar–opaque intergrowth replacing osumilite. (c) - XPL photomicrograph of a large twinned osumilite grain. (d) - BSE image of an osumilite–quartz intergrowth being replaced by a cordierite–K-feldspar± orthopyroxene intergrowth. (e) - BSE image of an osumilite–quartz intergrowth adjacent to orthopyroxene and quartz. See online version for colour.

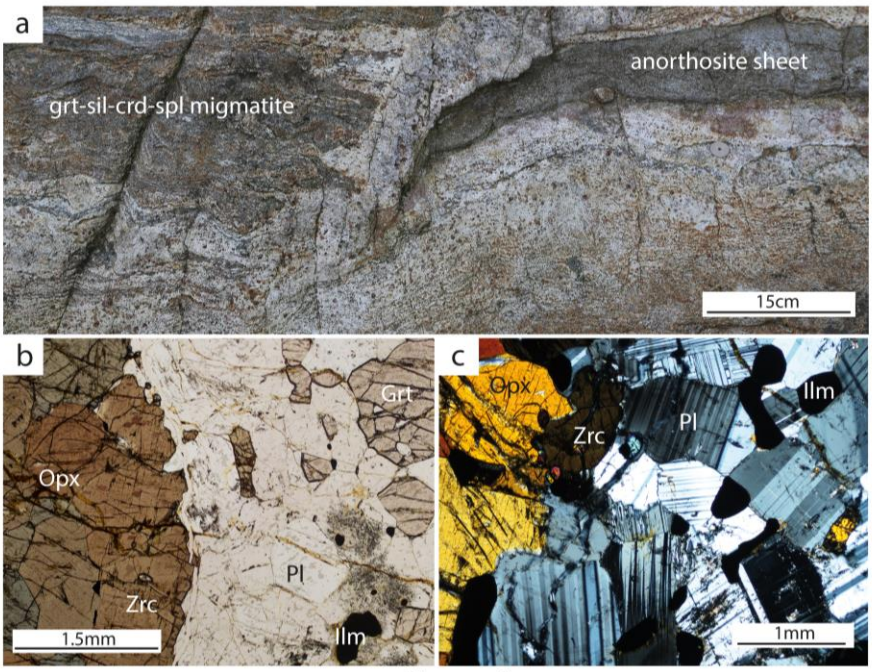

Figure 4

Figure 4: Field photograph and photomicrographs of ROG14/8, a garnet-bearing anorthosite sheet within a garnet–cordierite–sillimanite–spinel migmatite. (a) - Field photograph of the garnet-bearing anorthosite sheet aligned with the foliation of the surrounding garnet–sillimanite–spinel migmatite, (after Blereau et al., 2017). (b) - PPL photomicrograph of coarse-grained aggregates of orthopyroxene and garnet grains within a matrix of plagioclase. (c) - XPL photomicrograph showing plagioclase, orthopyroxene, ilmenite and zircon. See online version for colour.

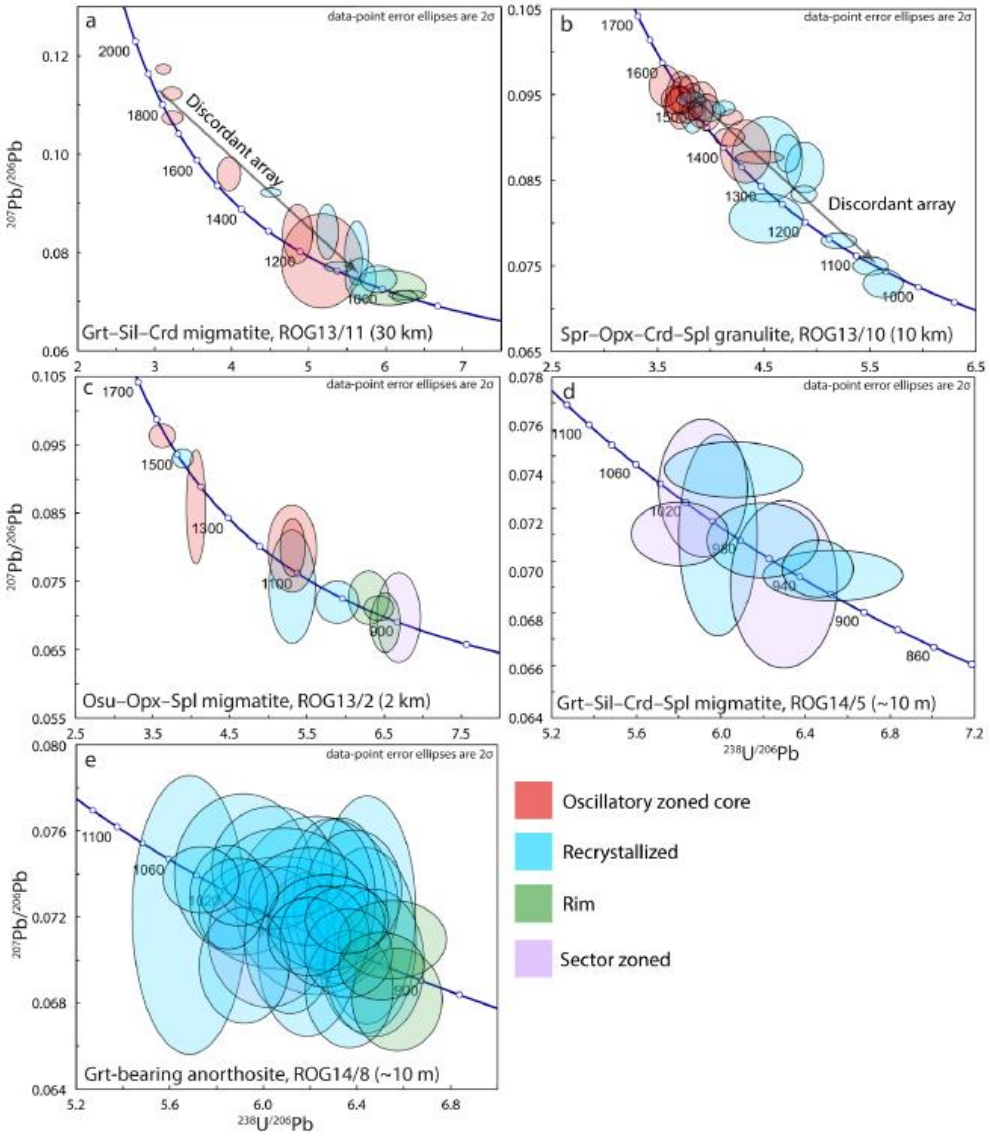

Figure 5: Zircon U–Pb concordia diagrams. Analyses are colour-shaded for the textural location of the analysis. See online version for colour.

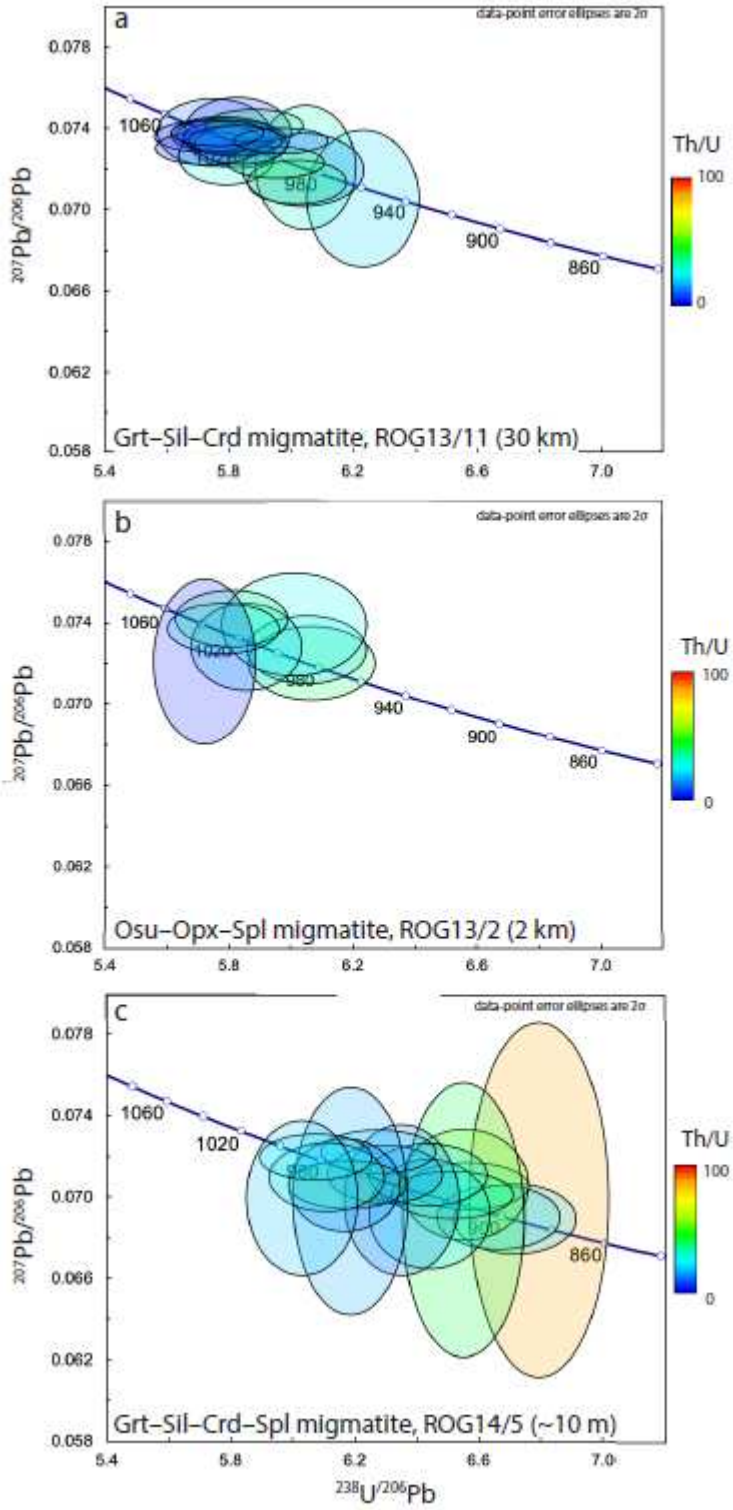

Figure 6: Monazite U–Pb concordia diagrams. Analyses are colour-shaded for Th/U content. See online version for colour.

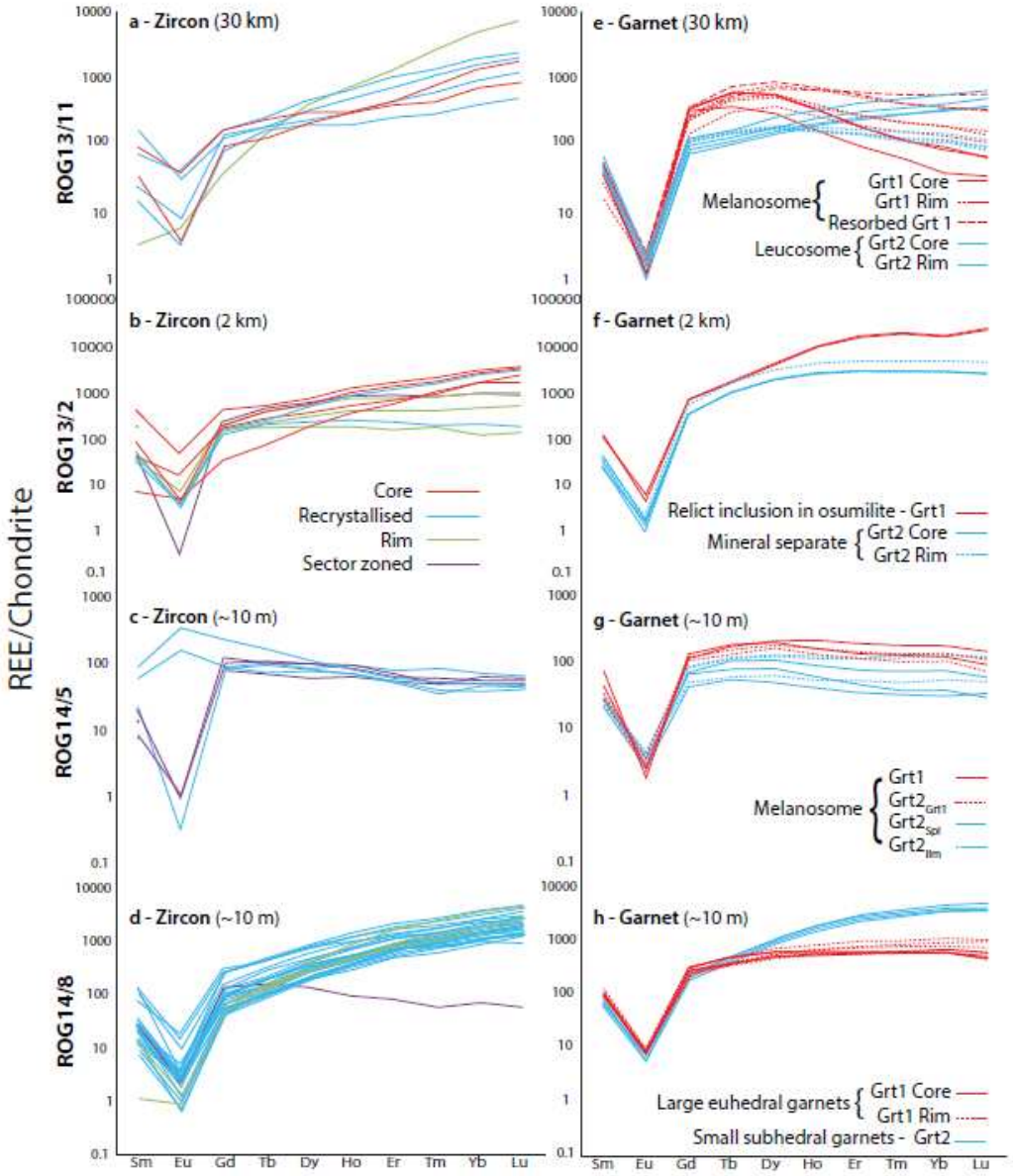

Figure 7: Chondrite normalised M-HREE plots for zircon (a–d) and garnet (e–h). Zircon and garnet REE analyses are colour-shaded to distinguish different textures/generations as explained in the text. See online version for colour.

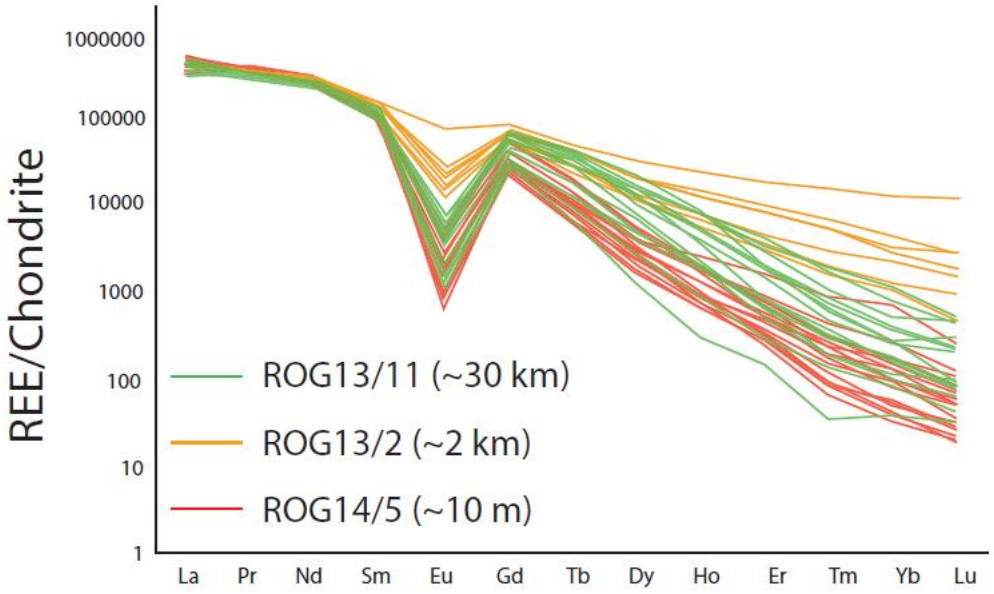

Figure 8: Chondrite normalised REE plot for monazite. See online version for colour.

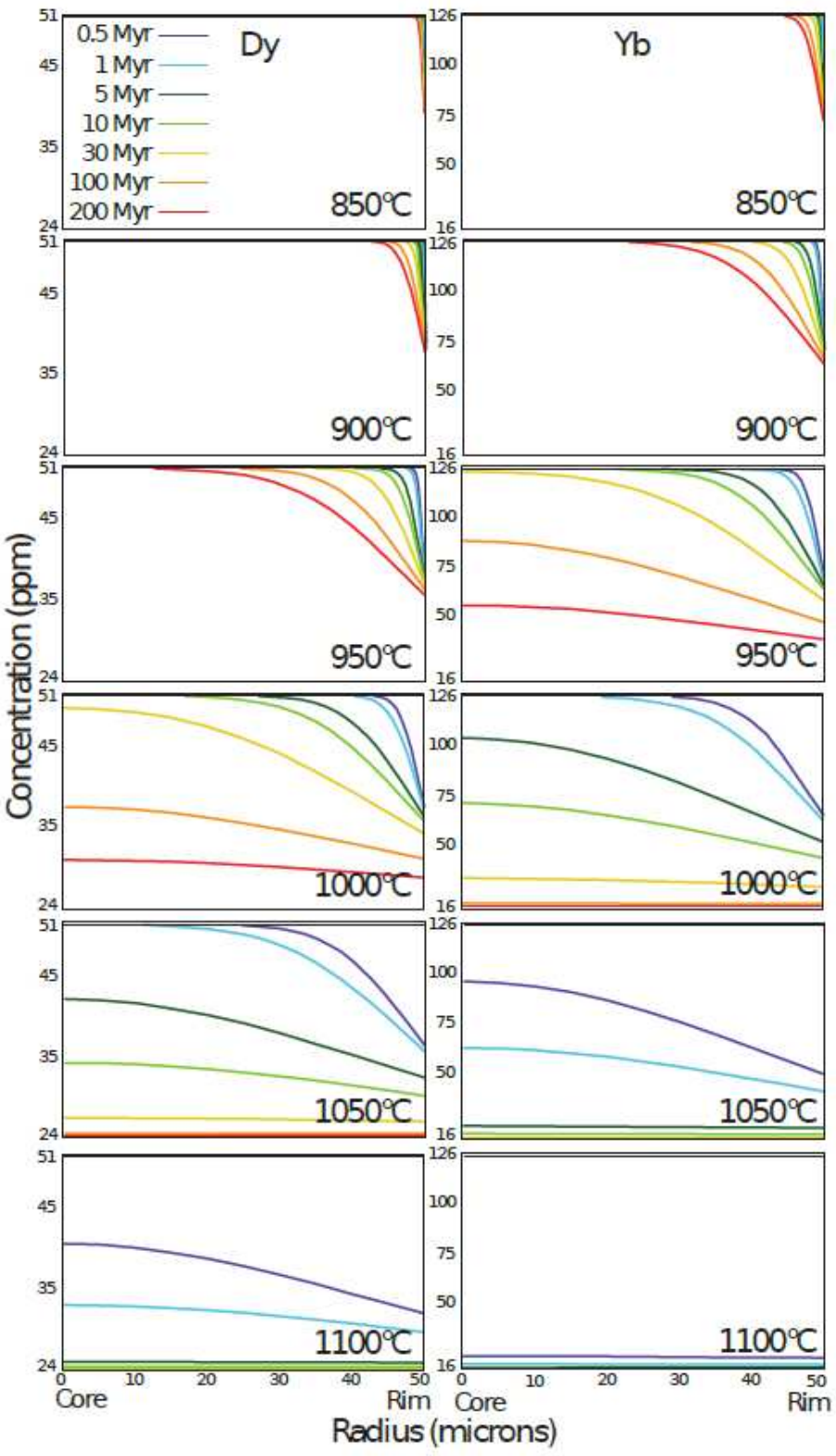

Figure 9: Modelled diffusion profiles of Dy and Yb in a theoretical zircon for different *T–t* scenarios. See online version for colour.

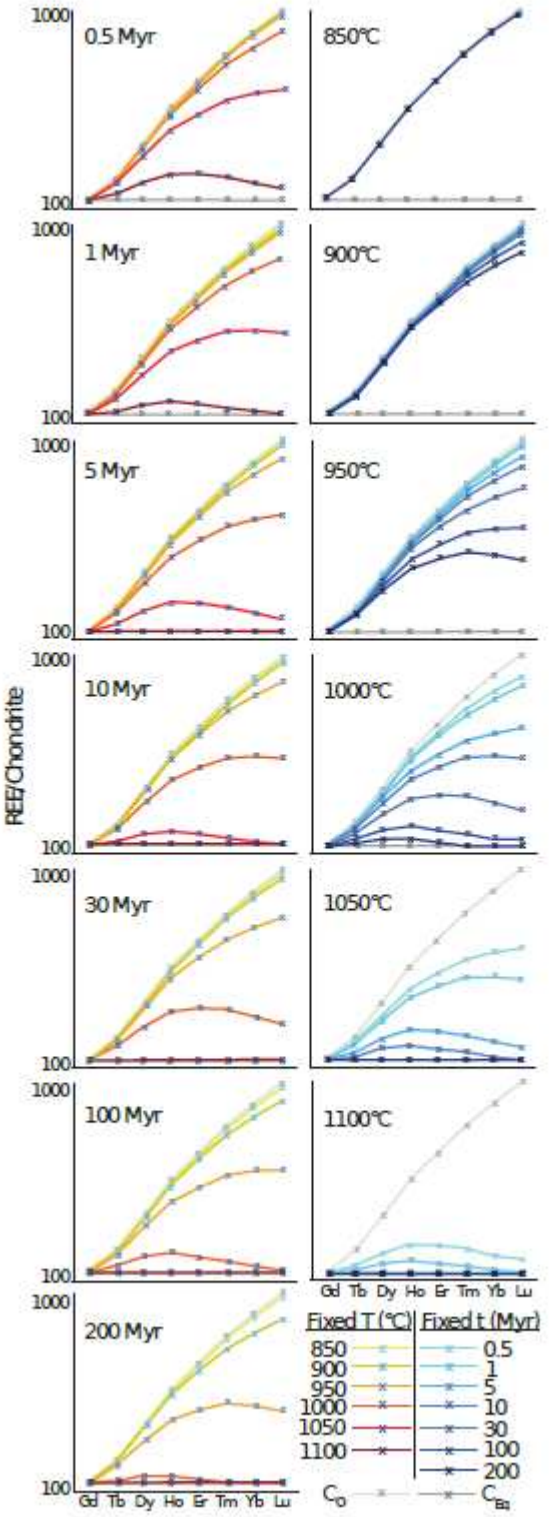

Figure 10: Diffusion-modified M–HREE compositions expected for a 20 μm diameter SHRIMP spot analysis on the edge of the modelled theoretical zircon. Compositions are given for set temperature or time periods. See online version for colour.

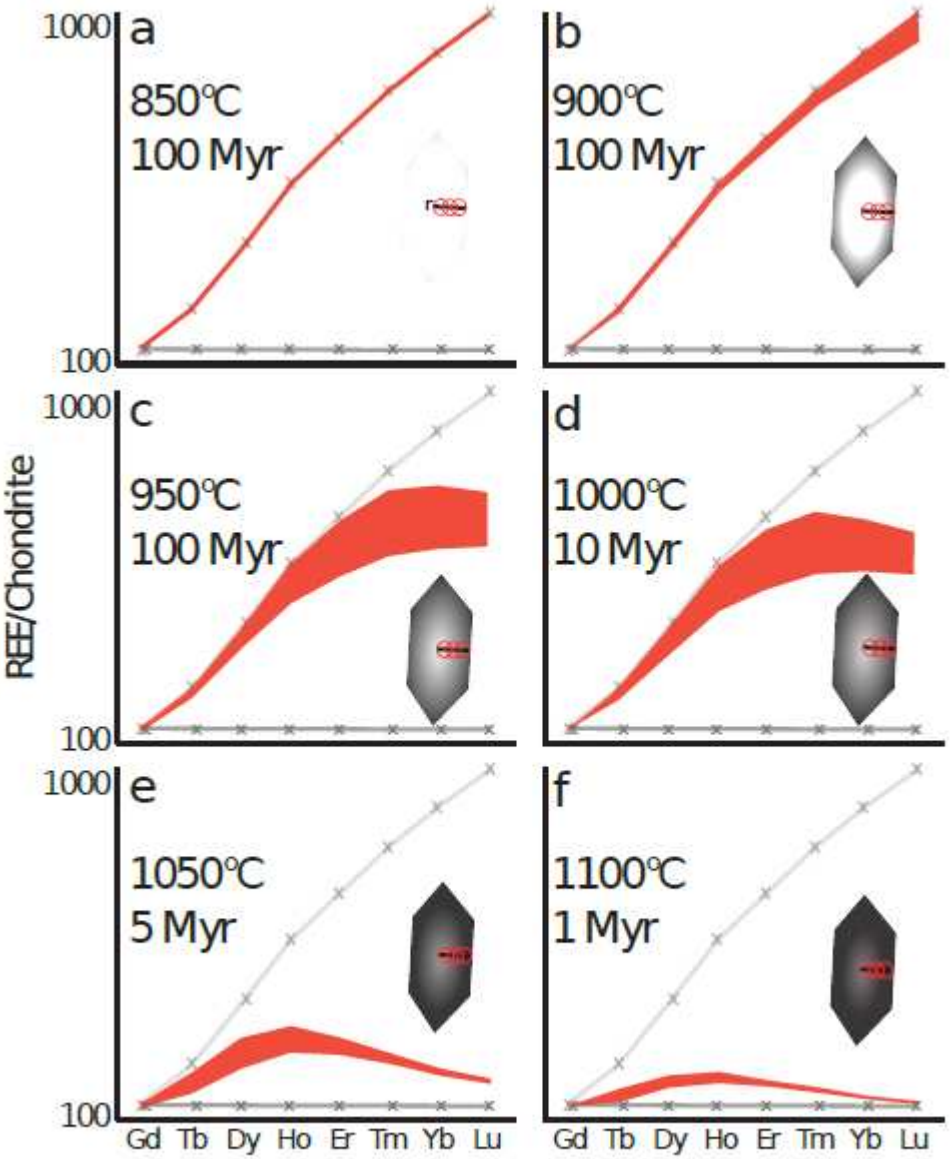

Figure 11: M–HREE spread generated through incomplete modification of the modelled zircon after different *T–t* scenarios and measured by multiple SHRIMP spot analyses. Shading on zircons illustrates the amount of REE modification, red circles represent 20 μm SHRIMP spots. The grey lines represent C_O (steep) and C_{Eq} (flat) compositions, *r*- modelled radius (50 μm).

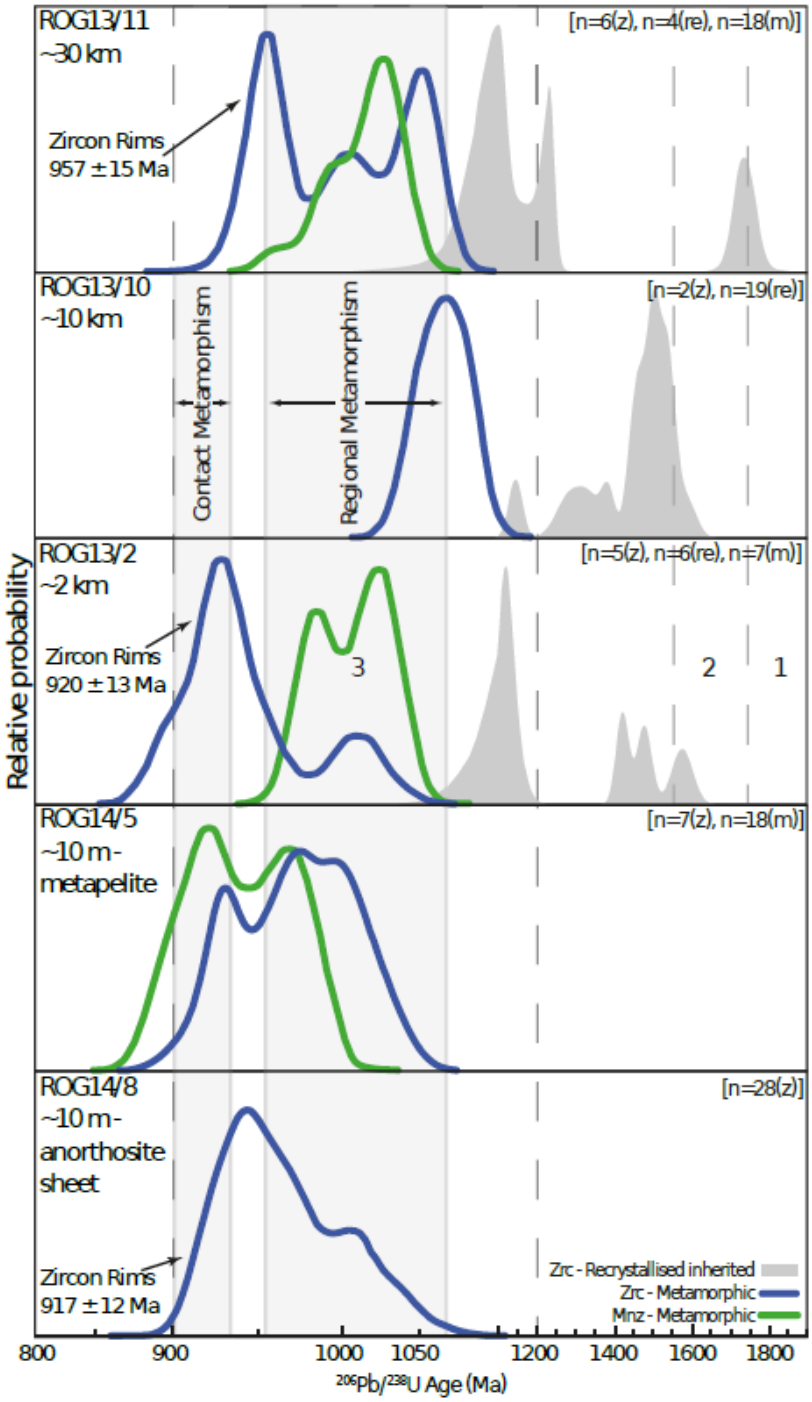

Figure 12: Relative probability plots of $^{206}Pb/^{238}U$ ages for all concordant U–Pb zircon and monazite analyses from this study. Samples are arranged according to their relative distance from the RIC (top plot is the farthest). All inherited and recrystallized zircon that may be partially reset are shown as filled grey plots; distinguished from zircon (of a range of textures) recording ages related to the onset of regional metamorphism and younger. Zircon rim ages are weighted mean $^{206}Pb/^{238}U$ ages. Numbers give timing of: 1 – Svecofennian Orogeny, 2 – Gothian Orogeny, 3 – Sveconorwegian Orogeny.

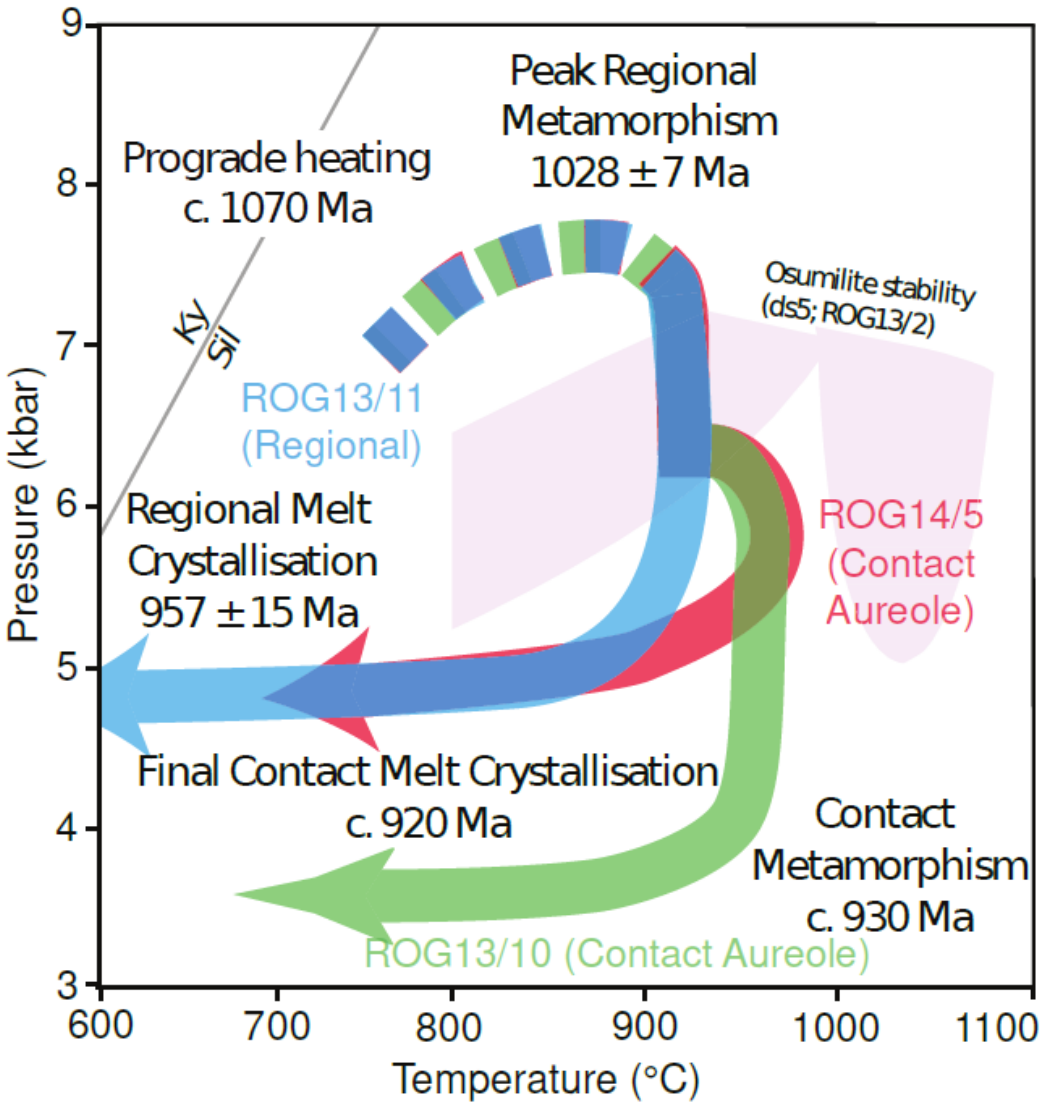

Figure 13: *P–T–t* evolution of the Rogaland–Vest Agder Sector, modified after Blereau et al. (2017). Osumilite stability for ROG13/2 (ds5) from Blereau et al., (2019).

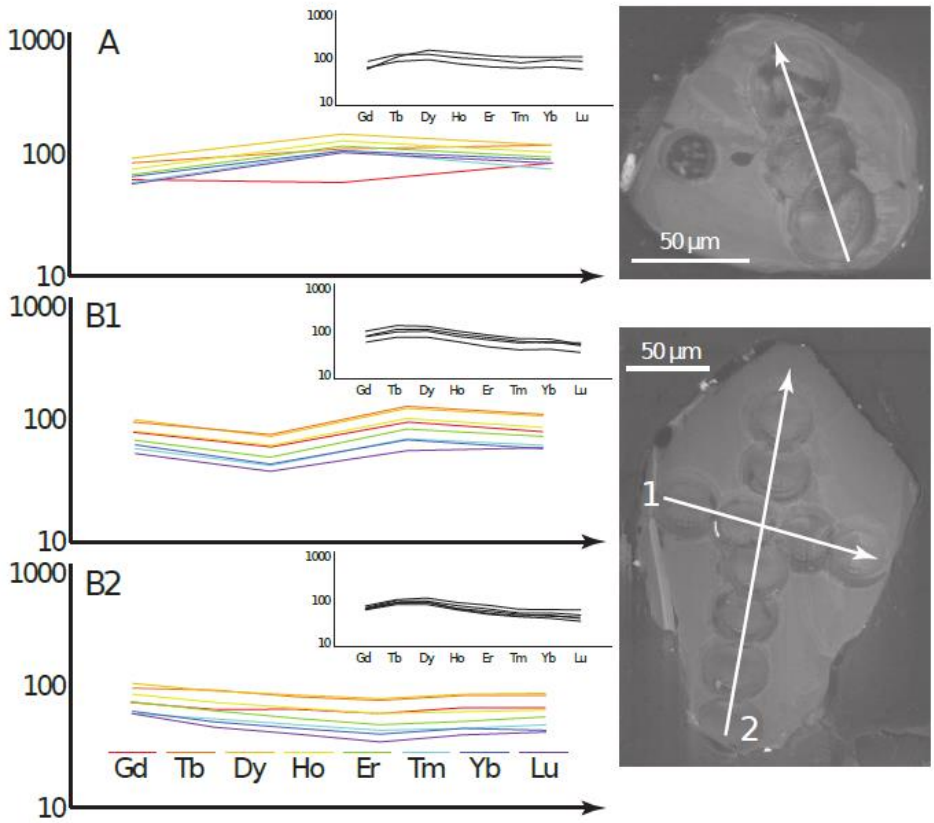

Figure 14: Laser M–HREE traverses in recrystallised zircons from ROG14/5 with profiles for each element across the traverse, M–HREE profile per spot and CL SEM image of the respective grains.

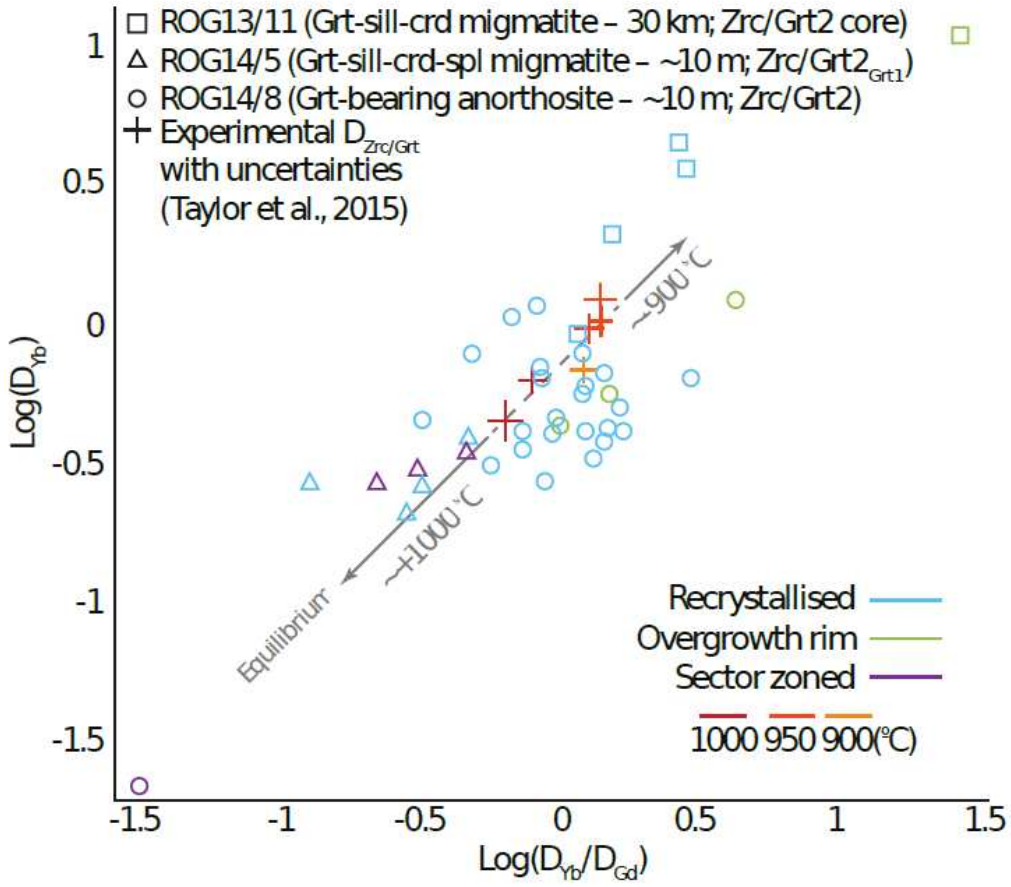

Figure 15: Zircon–Garnet REE array plot (Taylor et al., 2017) of HREE partitioning (D_{Yb} (zircon/garnet)) against M–HREE slope partitioning (D_{Yb} (zircon/garnet)/D_{Gd}(zircon/garnet)). $D_{Zrc/Grt}$ from the leucosome (Grt2 core) of ROG13/11 forms a scattered tangential trend towards the lower-T end of the experimental data experimental $D_{Zrc/Grt}$ data, interpreted as an older igneous population has recrystallized in the presence of garnet, but not fully re-equilibrated during regional metamorphism. $D_{Zrc/Grt}$ from ROG14/5 and ROG14/8 cluster over the high-T end of the experimental data. This supports the notion that the contact metamorphism was a more extreme thermal event. Sample ROG14/5 in particular suggests T in excess of 1000°C. The grey arrows show the expected temperature trends based on the current experimental data (Taylor et al., 2015). See online version for colour.

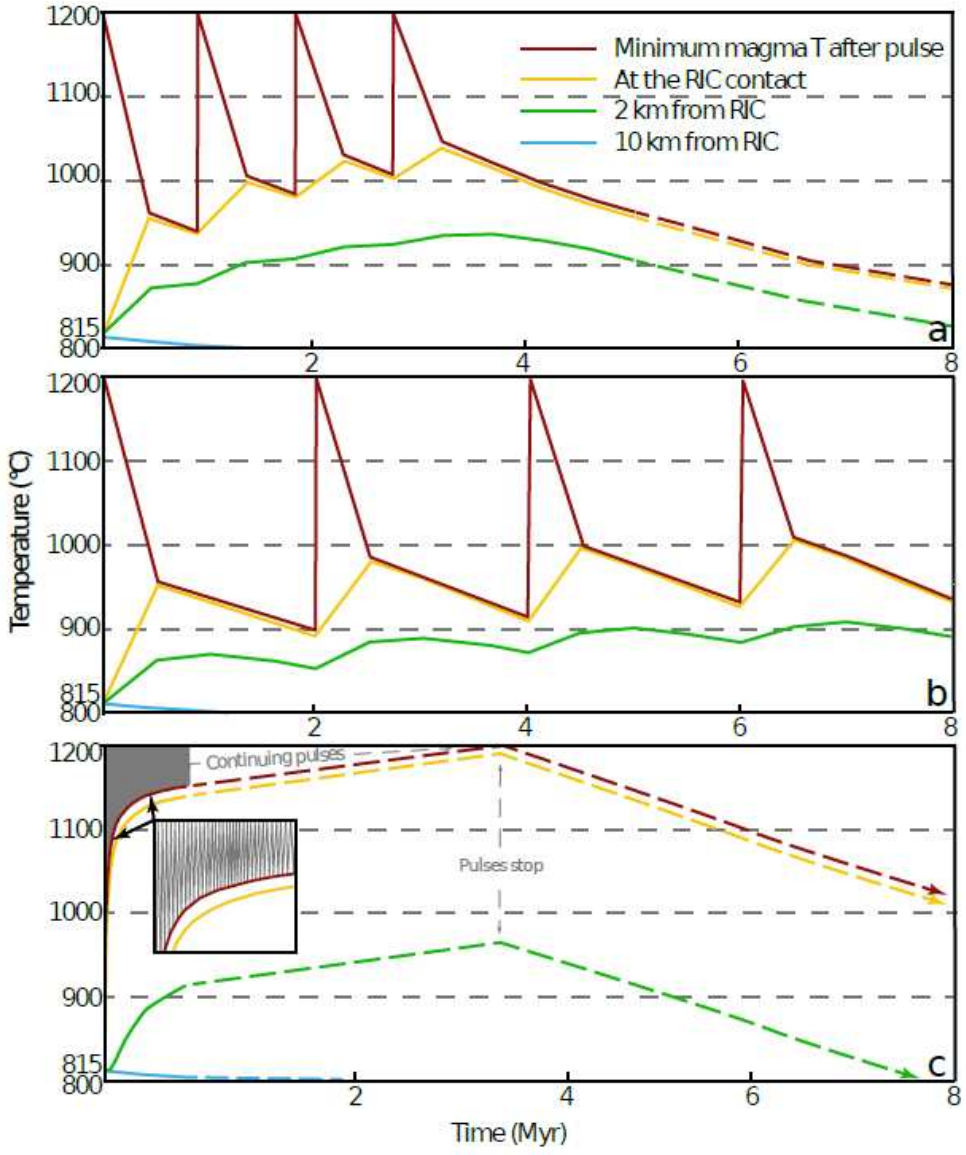

Figure 16: *T–t* paths from 2–D thermal models of possible emplacement mechanism of the RIC. (a) Magmatic pulse every 1 Myr, (b) Magmatic pulse every 2 Myr, (c) Incremental/multiple pulse scenario (pulse every ~10,000 years for the duration of the model, grey peaks at top of diagram). Dashed lines indicate extrapolation. See online version for colour.